



<b>Publication Year</b>	2017
<b>Acceptance in OA @INAF</b>	2021-02-12T15:43:42Z
<b>Title</b>	JIRAM, the Jovian Infrared Auroral Mapper
<b>Authors</b>	ADRIANI, Alberto; FILACCHIONE, GIANRICO; Di Iorio, Tatiana; TURRINI, Diego; NOSCHESE, RAFFAELLA; et al.
<b>DOI</b>	10.1007/s11214-014-0094-y
<b>Handle</b>	<a href="http://hdl.handle.net/20.500.12386/30366">http://hdl.handle.net/20.500.12386/30366</a>
<b>Journal</b>	SPACE SCIENCE REVIEWS
<b>Number</b>	213

# JIRAM, THE JOVIAN INFRARED AURORAL MAPPER

Alberto Adriani · Gianrico Filacchione ·  
Tatiana Di Iorio · Diego Turrini ·  
Raffaella Noschese · Andrea Cicchetti ·  
Davide Grassi · Alessandro Mura ·  
Giuseppe Sindoni · Massimo Zambelli ·  
Giuseppe Piccioni · Maria T. Capria ·  
Federico Tosi · Roberto Orosei · Bianca  
M. Dinelli · Maria L. Moriconi · Elio  
Roncon · Jonathan I. Lunine · Heidi N.  
Becker · Alessadro Bini · Alessandra  
Barbis · Luciano Calamai · Claudio  
Pasqui · Stefano Nencioni · Maurizio  
Rossi · Marco Lastrì · Roberto  
Formaro · Angelo Olivieri.

Received: date / Accepted: date

**Abstract** JIRAM is an imager/spectrometer on board the Juno spacecraft bound for a polar orbit around Jupiter. JIRAM is composed of IR imager and spectrometer channels. Its scientific goals are to explore the Jovian aurorae

---

The JIRAM project was started by Prof. Angioletta Coradini, Co-Investigator of the Juno Science team, who passed away on September 2011. During her life, she made seminal contributions to the exploration and the study of the Solar System and was a huge force in the development of Planetology in Italy. We dedicate this paper to her memory.

---

A. Adriani, G. Filacchione, T. Di Iorio, D. Turrini, R. Noschese, A. Cicchetti, D. Grassi, A. Mura, G. Sindoni, M. Zambelli, G. Piccioni, T. Capria, F. Tosi, R. Orosei  
IAPS/INAF, Via Fosso del Cavaliere 100, 00133-Roma, Italy  
Tel.: +39-06-45488365  
Fax: +39-06-45488383  
E-mail: alberto.adriani@iaps.inaf.it

B. M. Dinelli, M.L. Moriconi, E. Roncon  
CNR-ISAC, Bologna and Roma, Italy

J. I. Lunine  
Cornell University, Ithaca, NY, USA

H. N. Becker  
Jet Propulsion Laboratory, California Institute of Technology, Pasadena, CA, USA

A. Bini, A. Barbis, L. Calamai, C. Pasqui, S. Nencioni, M. Rossi, M. Lastrì  
Selex ES, Campi Bisenzio, Italy

R. Formaro, A. Olivieri. Italian Space Agency, Roma, Italy

and the planet’s atmospheric structure, dynamics and composition. This paper explains the characteristics and functionalities of the instrument and reports about the results of ground calibrations. It discusses the main subsystems to the extent needed to understand how the instrument is sequenced and used, the purpose of the calibrations necessary to determine instrument performance, the process for generating the commanding sequences, the main elements of the observational strategy, and the format of the scientific data that JIRAM will produce.

**Keywords** Juno · Jupiter · Image Spectrometer · Jovian Atmosphere · Jovian Aurorae

## 1 Introduction

IR imaging spectroscopy is a well-known remote sensing technique that has been used in the last decades in the exploration of the planets and satellites of the solar system. Among the outer planets, Jupiter was observed in the past by three other space-borne imaging spectrometers: NIMS, the Near Infrared Imaging Spectrometer [Carlson et al. (1986)] aboard Galileo mission; VIMS, the Visual and Infrared Mapping Spectrometer [Brown et al. (2004), Coradini et al. (2004)], during the Cassini mission 2000’s flyby of the giant planet; PERSI/Ralf, on board New Horizon mission to Pluto, has returned hyperspectral data of the Jupiter atmosphere during the spacecraft’s flyby in February 2007 [Reuter et al. (2007), Baines et al. (2007)]. JIRAM is tailored to obtain a detailed coverage of the Jupiter atmosphere from poles to equator taking advantage of the highly elliptical polar orbit of the Juno spacecraft. Differently from other spacecraft realized for the exploration of the outer solar system, Juno is a 2 *rpm* (12 *deg/sec*) spinning solar-powered spacecraft thus imposing challenging pointing and timing capabilities requirements for the onboard remote sensing payloads. Juno is the second of three NASA New Frontier missions and was launched in August 2011 to reach Jupiter in July 2016. The mission’s main scientific objectives are the study of the Jupiter’s aurora, polar magnetosphere, atmosphere and interior structure, with an overall goal to investigate the planet’s origin.

## 2 Scientific objectives

### 2.1 Auroras

The analysis of Jupiter’s auroras is one of the main scientific objectives for which JIRAM was built. Auroras are emissions of light at a range of wavelengths that result from high-energy electrons accelerated along the planet’s magnetic field and colliding with the upper atmosphere. Those emissions are spread over nearly the full electromagnetic spectrum, from X-ray to far IR wavelengths. Jupiter’s aurora is by far the most powerful among the planets

in the solar system. It is mainly generated by energy extracted from planetary rotation, though there seems to be a contribution from solar wind as well [Connerney and Satoh (2000)]. The study of the Jovian aurora will give us information about similar, though less energetic, phenomena on our own planet, but will also provide a model system for potentially observable phenomena associated with Jupiter-mass and super-Jupiter-mass exoplanets around nearby stars. Jupiter's polar auroras can be observed, at several wavelengths, as bright ovals that are off-center from the planet's geographical poles and co-rotate with the magnetic field. The major features of the Jovian auroras include a main oval and a region of patchy, diffuse emission within the branch on Jupiter's dusk side [Waite et al. (2000)]. The northern aurora in particular is very strong and is placed between  $165^\circ - 200^\circ$  longitudes, while the less prominent southern auroras are generally found between  $330^\circ - 90^\circ$  longitudes. In the main auroral structure, which is centered over the magnetic poles (the Jupiter's magnetic axis is tilted about  $10^\circ$  with respect to the rotational axis), the footprints of the emissions generated by the flux tubes of the satellites are present; those spots have fast dynamics that are driven by the orbiting satellites. Both northern and southern polar regions are subject to auroral emissions from the poles to latitudes around  $\pm 60^\circ$ , and some differences are apparent in the local dawn and dusk sectors. In the morning hemisphere, the emission is confined to a narrow arc structure, in the evening hemisphere the emission is more diffuse and broad. With the use of magnetospheric models, it is possible to correlate the auroral emission occurring in concentric ovals centered over the magnetic poles, to the magnetic field lines from 8 to about  $30 R_J$ . The electrons trapped and accelerated in the Jupiter magnetic field come from various sources, including Io's plasma torus, which is composed of sodium and sulfur particles released by the satellite's volcanic emissions.

Among the various molecular ions that undergo emission in Jupiter's aurora,  $H_3^+$  is the one emitting in the JIRAM spectral range. This ion is formed at the base of the exosphere through the reaction  $H_2^+ + H_2 \rightarrow H_3^+ + H$ . The resulting  $H_3^+$  has a complex roto-vibrational structure of energy levels and two distinct populations ( $I=3/2$ , ortho;  $I=1/2$ , para). The main roto-vibrational band is the  $0 \leftarrow \nu_2$  around  $2521 \text{ cm}^{-1}$ , which is composed of more than 200 possible transitions in the range  $3.0\text{--}5.0 \mu\text{m}$  [Lindsay and McCall (2001)]. Observation of the infrared emission of  $H_3^+$  is possible because it is in a spectral interval coinciding with a strong methane absorption band falling between  $3.2$  and  $4.0 \mu\text{m}$ . At these wavelengths, the solar and thermal radiance emitted by the planet is very low, and auroral emissions will have a high contrast with respect to Jupiter's disk, which is very dark due the methane absorption. The JIRAM instrument, as described in greater detail in section 3.1, has been designed to investigate the weak  $H_3^+$  infrared emission and will be able to furnish spatial, spectral and temporal distribution of the Jovian auroras. Moreover, since observations of the  $H_3^+$  emission by limb measurements allow the study of the aurora's distribution in the thermosphere, JIRAM shall be able to indirectly contribute to the mapping of the Jovian magnetic field.

## 2.2 Hot spots and atmospheric component gases retrieval

The optical surface of Jupiter is dominated by ammonia clouds. At deeper tropospheric levels, between 1 and 10 *bar*, water dominates as the principal condensate. Hence, the nature of convective transport is different between that at levels above and below. Understanding the nature of moist convection [Ingersoll et al. (2000)], lightning, cloud formation [Stoker (1986)], and transport of disequilibrium species [Vischer and Fegley (2005)] requires observations that reach below the layer of ammonia clouds and into this minimally explored deeper troposphere, where moist convection may be the dominant factor in converting the internal heat flow into atmospheric kinetic energy [Gierasch et al. (2000)]. Investigation of these regions will require the use of an entry probe such as Galileo at multiple sites, or remote sensing from close orbit and at wavelengths that can penetrate to the appropriate pressure levels. This last approach is the one we plan to achieve with JIRAM.

Hot spots, which were originally discovered by ground-based observations [Ortiz et al. (1998)], are regions on the disk of Jupiter where thermal radiation escapes from pressure levels (depths) larger than the average emission levels. Higher atmospheric emission levels are mostly determined by the opacity of widely spread ammonia clouds. Such features are thought to be areas of downwelling and, hence, dry (low ammonia and water humidity) air. Many hot spots occur in a zone between the equator and 15° north latitude, the North Equatorial Belt (NEB), but excess thermal radiation is seen from much of the planet, which suggests clearings in the clouds below the spatial resolution of ground-based observations. While resolvable hot spots cover a maximum of 0.5% of Jupiter's surface, they dominate the planet's thermal emission at wavelengths around 5  $\mu\text{m}$ . Ortiz et al. (1998) found that the latitude and drift rate of some observed hot spots are consistent with formation by an equatorially trapped Rossby wave of meridional degree 1 moving with a phase speed of  $\sim 100 \text{ m/s}$ . It is doubtful, however, that all hot spots over all spatial scales form following a simile process [Friedson and Orton (1999)].

Because of their relative lack of gaseous and cloud opacity from water and ammonia, hot spots are windows into the deep atmosphere and allow to probe the properties of the atmosphere down to 5-6 *bar* in the 4-5  $\mu\text{m}$  low opacity spectral region [Roos-Serote et al. (2004); Ortiz et al. (1998); Terrile and Westphal (1977)]. Understanding the morphology of the hot spots in a three dimensional sense, which would require observation as a function of wavelength, and particularly the morphology at deeper pressure levels, where the drier air of hot spots may be remixing with moister ambient air, will help to answer questions as to why hot spots form and what role they play with regard to transport of energy and condensable species within the Jovian atmosphere. However, of equal or greater importance is mapping of variations in the moisture content of the air on smaller scales from hundreds to thousands of kilometers the realm of mesoscale convective complexes seen by Galileo SSI observations, which are indicative of low level convergence of air near the base of the water clouds [Gierasch et al. (2000); Roos-Serote et al. (2004)].

Sounding in the near-infrared between 2.0 and 5.0  $\mu m$  by an orbiting spacecraft will be necessary to determine the deep morphology of water clouds that characterize storms and, hence, moist convective processes [Atreya et al. (2005)]. Three-dimensional mapping of water variations and cloud morphology will quantify the nature of water moist convection. The vertical heat flux through a single large mesoscale convective complex on Jupiter may be comparable to the total internal energy flux from deep inside Jupiter [Gierasch et al. (2000)], and so such mapping will yield important insights into how thermal energy is converted to atmospheric turbulence and, ultimately, escapes from Jupiter's interior. Because JIRAM is essentially an infrared mapper imager joint to a 2-5  $\mu m$  imaging spectrometer, it has the capability to address this important scientific objective. For the JIRAM baseline, a 4000-km scale moist convective mid-latitude storm system, such as that observed by Galileo, can be mapped at a maximum spatial resolution of 10  $km/pixel$ , and spectroscopically resolved over hundreds of wavelength channels in the 2-5  $\mu m$  range, which would allow the profiling of moist convective columns and the dry intervening regions of subsidence with excellent horizontal and vertical resolution. Finally, thermal emission spectra in the 4.5 to 5.0  $\mu m$  region (around the center of a spectral window free of  $CH_4$  absorptions) show features attributed to minor constituents that are present in the Jovian troposphere, specifically water vapor ( $H_2O$ ), ammonia ( $NH_3$ ), phosphine ( $PH_3$ ) as well as germane ( $GeH_4$ ) and deuterated methane ( $CH_3D$ ). Mapping their vertical variation has been demonstrated to be a fruitful technique: Cassini VIMS instrument achieved similar results on Saturn, and JIRAM will do the same at Jupiter. The structure and dynamics of the Jovian atmosphere are characterized by the presence of a large variety of clouds at different altitudes. A layer of visible clouds composed of ammonia crystals is located at a pressure level of about 1 bar, while clouds beneath that level appear to be composed of ammonium hydrosulfide ( $NH_4SH$ ) and water. Moreover a specific atmospheric chemistry is responsible for the formation of compounds with greater complexity, probably involving organic polymers. Their production is assumed to be driven by solar ultraviolet light, lightning discharges, and charged particles raining down from the magnetosphere in the polar regions.

Ammonia clouds have been observed only in very limited number and areas [Baines et al. (2003)] and, following Atreya et al. (1999) and Atreya et al. (2005), these clouds would be ubiquitous on Jupiter, their observation being difficult as their original signature is masked by the effect of the stratospheric hydrocarbon aerosols, that sediment and mix with clouds.  $NH_4SH$  clouds, that form as a result of a reaction between  $NH_3$  and  $H_2S$  gases, have never been observed.  $H_2O$  clouds are expected deeper in the atmosphere at pressures where water reaches its saturation values.

Observations from the Voyager [Conrath and Gierasch (1986)], Galileo [Banfield et al. (1998); Irwin et al. (2001); Simon-Miller et al. (2001)] and Cassini [Matcheva et al. (2005)] missions and successive analyses [Sromovsky and Fry (2010a); Sromovsky and Fry (2010b)] are consistent with thermo-chemical models, which predict the composition of topmost and next lower cloud layers

to be  $NH_3$  and  $NH_4SH$ , respectively, whereas the observations of lightning from Galileo and Cassini associated with thunderstorms at pressures of 3 *bar* or greater [Gierasch et al. (2000)] are consistent with model predictions of water clouds deeper in Jupiter's atmosphere [Weidenschilling and Lewis (1973); Atreya and Romani (1985); Stoker (1986); Atreya et al. (1999)]. JIRAM [Adriani et al. (2008)] on Juno will measure thermal emission from Jupiter's atmosphere in the 2-5  $\mu m$  spectral range, which would permit the identification of ammonia in the clouds. Moreover at 5  $\mu m$  the imager will allow study of those areas where the cloud deck is sufficiently optically thin to sound the lower levels. JIRAM could observe the  $NH_4SH$  and water clouds in localized areas characterized by updrafts.

Jupiter's cloud system is a good proxy of the complexity of its atmospheric circulation. Using them as tracers, wind velocities at different pressure levels, depending on the sounding wavelengths, have been estimated by means of the analysis of long time series of observations. Zonal winds at pressure levels of approximately 0.7 -1 *bar* have been studied by Ingersoll et al. (2004) and Adriani et al. (2011). The former indicated a quite stable pattern between the two previous missions Voyager [Limaye (1986)] and Cassini [Porco et al. (2003)] while the latter showed a little increasing in the peak velocity near the northern tropical region analyzing Cassini and the Wide Field Planetary Camera 2 (WFPC2), on the Hubble Space Telescope (HST), images taken in the 2000-2008 period. With its imager, JIRAM will sound atmospheric levels deeper than 1*bar* where the clouds are relatively thin, i.e. mainly in the belts, possibly measuring the winds below the cloud deck in the visible spectral range. Unfortunately the observations of the planetary dynamical features and their evolution will suffer from time limitations imposed by the planned orbits and the mission schedule.

### 2.3 Implications for Origins

The enrichment in noble gases and in the  $C, N, O, S$  chemical elements with respect to the solar abundances measured by the Galileo probe in the atmosphere of Jupiter [Owen et al. (1999)] has been identified as a legacy of the formation process of the giant planet (see e.g. Lunine et al. (2004) and references therein). Recently, Helled et al. (2011) argued that the Jovian enrichment in volatiles and noble gases does not directly reflect the particular mode of formation of Jupiter – that is, by core accretion versus disk instability – but instead supplies information on the environment (i.e. temperature, pressure, composition) within which Jupiter formed.

Both volatile and refractory materials may have been delivered to the forming giant planet from different sources. Gautier et al. (2001) suggested that the noble gases and the  $C, N, O, S$ -rich volatiles were trapped in the form of solid clathrate hydrates in the planetesimals that formed in the cooling feeding zone of Jupiter and were delivered to the giant planet following their capture and dissolution in its atmosphere. Owen et al. (1999) invoked instead planetesimals

that had adsorbed volatiles at very low temperature. More recently, Guillot and Hueso (2006) suggested that the enrichment in noble gases can be explained solely through the late accretion of gas by Jupiter from a chemically evolved solar nebula, in which *Ar*, *Xe* and *Kr* settled toward the mid-plane of the nebula together with the solid material while *H*, *He* and *Ne* photo-evaporated. This scenario, however, does not explain the observed enrichment in the other volatile species (*C*, *N*, *O*, *S*). Finally, Lodders (2004) and Mousis et al. (2012) proposed non-solar, carbon-rich or oxygen-depleted compositions for planetesimals that contaminated Jupiter; the latter showed this fit Galileo measurements [Wong et al. (2004)] as well as the solar *C/O* models.

The composition of the planetesimals in the circum-solar disk that can be accreted by Jupiter, however, is not the only parameter that can affect the composition of the giant planet. The formation of Jupiter, in fact, changes the local conditions existing at its formation region [Coradini et al. (2010)]. The gas accretion causes the forming planet to acquire an accretion luminosity that heats up the disk and causes the vaporization of most volatile species [Coradini et al. (2010)]. Moreover, the accretion process also affects the gas density and velocity in the feeding zone of the giant planet and thus influences its pressure and the possibility for volatile species (*H<sub>2</sub>O*, *NH<sub>3</sub>*, *CO*, *CO<sub>2</sub>*, *CH<sub>4</sub>*) to condense (or re-condense) as solids [Coradini et al. (2010)]. Finally, the evolution of the circum-Jovian environment would influence also the formation of the satellite system of the giant planet (by affecting the capture and migration rates of planetesimals in the circum-planetary disk) and the abundance of volatile elements in their bulk composition.

In principle, planetesimals could be captured by Jupiter not only during its formation process but also over most of its history. However, once it reaches its final mass Jupiter is more efficient in ejecting the planetesimals from the Solar System than in accreting them [Weidenschilling (1975), Guillot and Gladmans (2000)]. Moreover, the flux of material crossing the orbit of the planet rapidly decreases with time. After its formation, Jupiter can undergo a phase of late accretion while the other giant planets are still forming [Safronov (1972), Weidenschilling (1975), Turrini et al. (2013)] and later while the terrestrial planets form [Guillot and Gladmans (2000)]. The captured planetesimals, however, would enrich the planet by about 1  $M_{\oplus}$  of high-*Z* material, as an order of magnitude [Guillot and Gladmans (2000), Turrini et al. (2013)]. At the time of the Late Heavy Bombardment, the same enrichment would be of only 0.15  $M_{\oplus}$  [Matter et al. (2009)].

It is therefore plausible that the bulk of the Jovian enrichment dates back to the time of the formation of the giant planet and is linked to the role of the circum-Jovian disk in capturing planetesimals from the solar nebula. As the composition of the circum-solar and circum-Jovian disks and the abundances of the different elements and the chemical species vary with time and the disk opacity (see e.g. Dullemond et al. (2007), Bergin et al. (2007), and Coradini et al. (2010)), the study of the composition and the abundances of the chemical species in the Jovian atmosphere that JIRAM will perform has the potential to supply valuable information on the timescale over which formation occurred



and the environment from which the planet and its satellites were generated. The possibility of constraining the formation environment, and therefore the extent of the possible migration of Jupiter [Turrini et al. (2011), Walsh et al. (2011)], is particularly important to improve our understanding of the evolution of the Solar System at the time of the solar nebula. Migration might in fact imply a different atmospheric composition with respect to the standard scenario. Further discussion of formation models is given in the chapter by Owen et al. (1999), but it is clear from the foregoing that compositional measurements by JIRAM will help illuminate the early history of the solar system.

### 3 Instrument Description

JIRAM relies on the solid heritage coming from the Italian-made visible and near infrared imaging spectrometers realized in the past years like VIMS aboard Cassini [Brown et al. (2004)], VIRTIS-M aboard Rosetta [Coradini et al. (2007)] and Venus Express [Piccioni et al. (2007)], and VIR-MS aboard Dawn [De Sanctis et al. (2011)]. However, JIRAM has different constraints that make this instrument unique among the others of its family. In first place, Juno is not a three-axis stabilized platform like the previous mentioned missions but it is a spinning spacecraft. This architecture made necessary to develop a different concept of the instrument that needs to operate while the spacecraft is rotating around its axis. To adapt the instrument to such platform we have introduced a de-spinning flat mirror at the telescope's entrance pupil; this mirror uses a mechanism that allows to rotate it synchronously with the rotation of the spacecraft in order to counter-compensate the spin motion. The spinning rate of the spacecraft is planned to be around  $2rpm$ , an angular velocity of  $12deg/s$ , during the mission phase at Jupiter. The instrument will use the dynamical information from the spacecraft to compute its counter-compensating speed velocity as well as the pointing direction. Due to the relative fast angular speed of the spacecraft, the action of the de-spinning mirror had to be limited, heading to a maximum time in which the target scene can be kept still: this time is  $1.1s$ . Secondly, JIRAM is operating in a limited range of infrared wavelengths,  $2-5\mu m$ , and it is essentially composed by two channels, a slit spectrometer and an imager, sharing the same telescope, the de-spinning mirror and the internal calibration unit. The spectrometer's slit is co-located in the imager's *FOV*. Finally, the instrument's optical and electronics components were chosen and designed to operate in the harsh Jovian radiation environment while maintaining a reduced mass ( $12.9kg$ ) and power consumption (average  $16.4W$ ). The instrument has been realized by Selex ES (Campi Bisenzio, Italy) under an ASI (Italian Space Agency) contract. INAF-IAPS, Rome, has the scientific responsibility of the experiment.

### 3.1 The instrument

Figure 1 shows the optical head of the instrument. The optical layout (Figure 2, Figure 3, and Figure 4) is based on a modified Schmidt telescope (equivalent  $F = 160mm$ ,  $f/\# = 3.7$ , equivalent aperture  $44mm$ ). Thanks to a



**Fig. 1** Instrument's optical head.

beam splitter, the optical beam is divided between the imager channel (hereafter IMG) and the spectrometer channel (SPE) with an efficiency ratio of 30 – 70%, respectively. Both the imager and the spectrometer channels use Hybrid Thinned HgCdTe photodiodes on CMOS ROIC focal planes with the same characteristics:  $270 \times 438$  pixels arrays,  $40 \times 40 \mu m$  pixel pitch, about 2 millions e-full well capacity. The imager focal plane is furthermore divided in two equal areas defined by the superimposition of two different band-pass filters: filter L, centered at  $3.455 \mu m$  with a  $290 nm$  bandwidth; filter M, centered at  $4.780 \mu m$  with a  $480 nm$  bandwidth; each channel has a Field of View ( $FOV$ ) of  $1.75^\circ \times 5.94^\circ$  ( $128 \times 432$  pixels corresponding to the along by across track directions) and an Instantaneous Field of View ( $IFOV$ ) of about  $250 \times 250 \mu rad$ . An opaque region of dimension equivalent to about 10 pixels separates the two filters. The L-channel is designed to obtain high resolution images of the polar auroras by selecting the  $H_3^+$  emissions while the M-channel is suited to image the deeper atmosphere, in particular hot spots. The spectrometer channel is able to realize co-located imaging spectroscopy in the  $2.0$ - $5.0 \mu m$  range in the M-filter channel  $FOV$  by using a slit 256 samples-wide with a  $FOV$  of  $3.52^\circ$  and an  $IFOV$  of  $250 \mu rad$ . SPE uses a quasi Littrow configuration where a flat grating ( $30.3 grooves/mm$ ,  $2.56^\circ$  blaze angle) is used to disperse the slit's image across the focal plane. Thus the instantaneous acquisition of the detector is made of 336 images of the slit taken along the detector's columns in the spectral range  $2$ - $5 \mu m$  with a spectral sampling of about  $8.99 nm/band$ . The SPE focal plane is equipped with two order sorting filters having the junction (dead zone) located around  $3.7$ - $3.8 \mu m$ . Finally, aberrations in the telescope and in the spectrometer are corrected thanks two dioptric doublets.

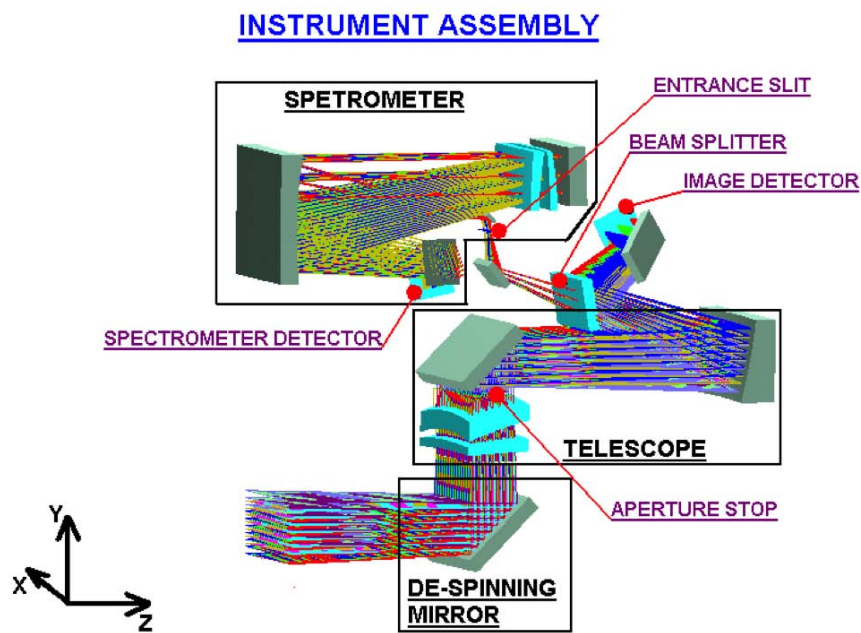


Fig. 2 Optical layout of the instrument.

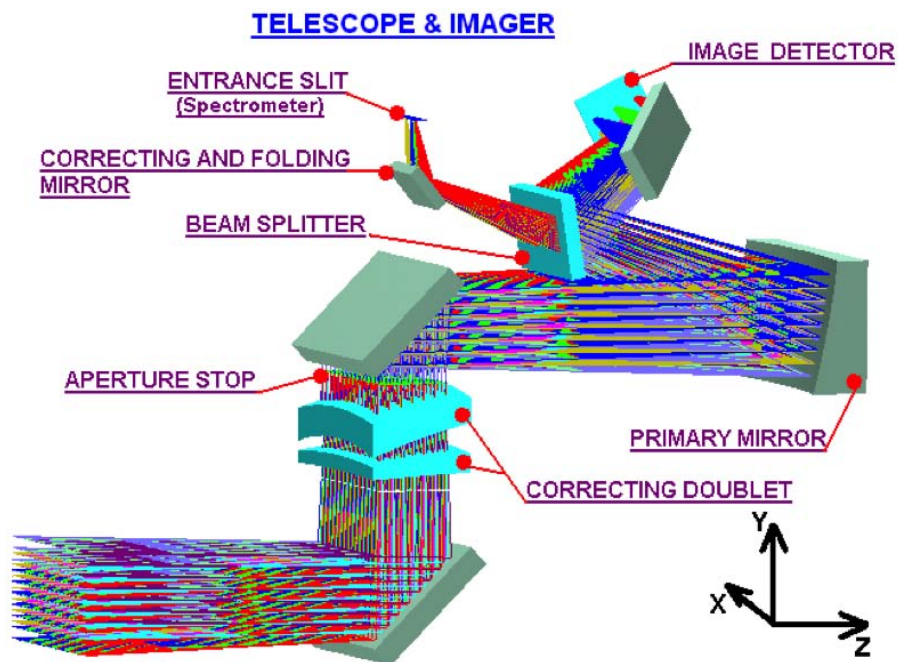
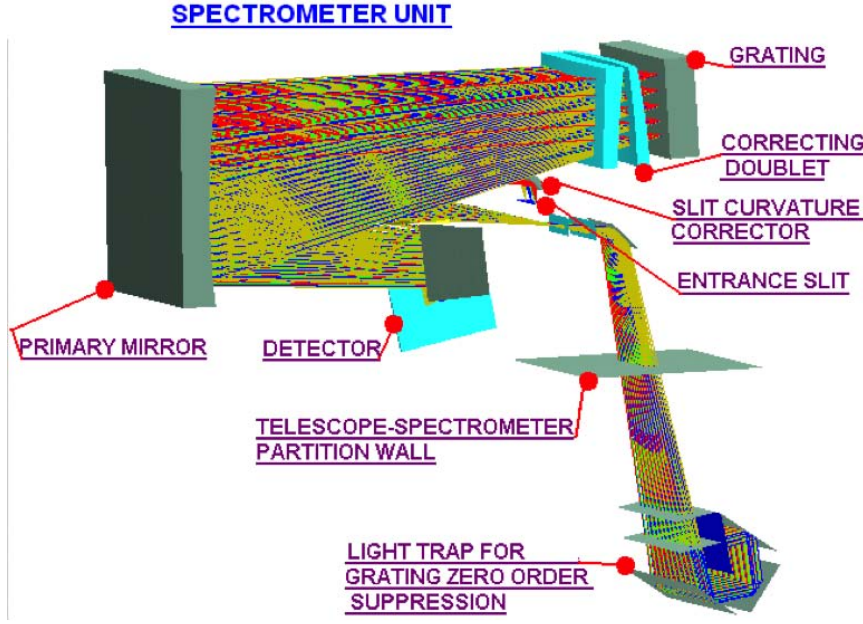


Fig. 3 Optical layout of telescope and imager.



**Fig. 4** Optical layout of spectrometer.

The JIRAM's optical head is passively cooled and it is mounted on the aft deck of the spacecraft to assure that the instrument is in shade during all the mission phases in which its operability is requested. The instrument is equipped with two external radiators, one of them is closely linked to the detectors and it is used to passively cool down the two focal planes to about 80K. The second one is coupled to the optical bench structure (telescope, spectrometer) in order to guarantee an operative temperature of about 120K or less. At these temperatures the instrumental performances are optimized, meaning that the detector dark current and the instrumental internal background are minimized. The instrument is connected to the spacecraft through an interface sub-plate to increase its thermal insulation. The sub-plate also protects the optical head from the sun illumination for spacecraft-sun angles lower than  $14^\circ$ . During the mission when JIRAM is going to operate at Jupiter the off-sun angle will be always lower than  $10^\circ$ . Finally, a separate Main Electronics box houses the power and distribution unit, the data processing unit and data compressor, the de-spinning mirror driver and the data/power connections towards the optical head and the spacecraft interface bus.

### 3.2 Internal calibration unit and blackbody sources.

An internal calibration unit (ICU) is placed on the structure of the telescope's entrance baffle (see Figure 5). It consists of a collimator coated with a golden diffusive coating and by two IR emitters that illuminate it. By aligning the de-

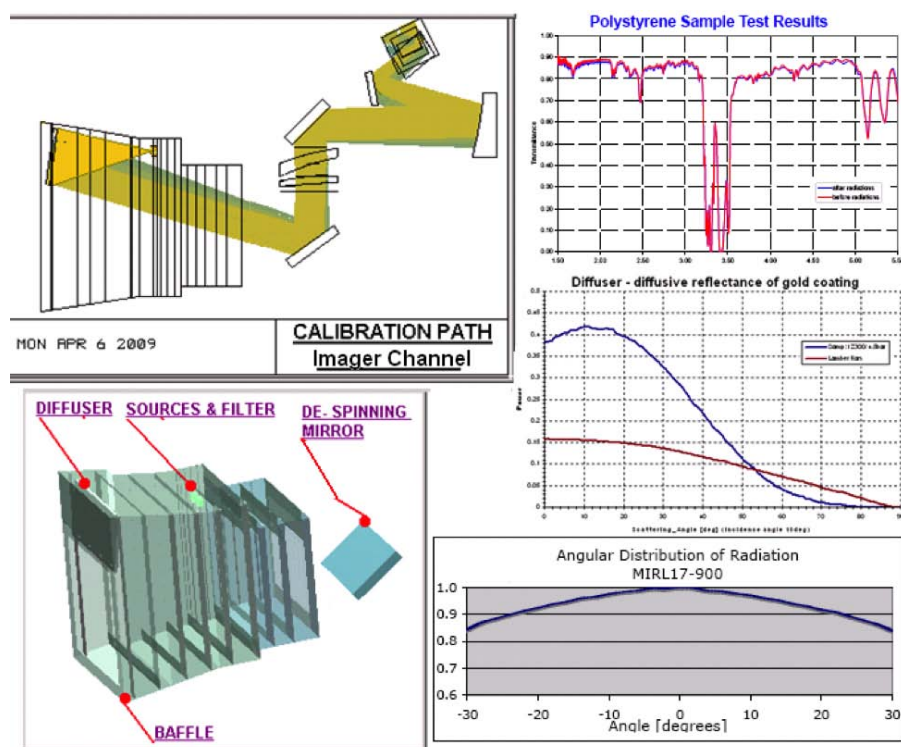


**Fig. 5** The Internal Calibration Unit (ICU). Upper left panel: light path from the internal calibration sources to the imager, the despinning mirror when placed in a proper position serves the ICU by directing the light inside the instrument; lower left panel: location of the ICU on a side of the entrance baffle of the instrument and the relative position of the despinning mirrors; upper right panel: spectral characteristic of the polystyrene filter placed in front of the calibration sources for performing internal spectral calibration; middle right panel: diffusing power of the golden diffuser versus the diffusing angle (blue curve), compared with regular lambertian diffusion (red curve); lower right panel: angular distribution of the diffused light.

spinning mirror to the ICU axis and switching on the sources, the instrument is able to periodically acquire a reference signal useful to check the relative radiometric and spectral responses.

ICU uses two infrared sources for redundancy. The infrared light sources are fabricated using Micro-Electro-Mechanical Systems (MEMS) technology. They have high emissivity and high thermal conductivity, and the low thermal load of the membranes allows rapid heating and cooling. An image of the IR emitters and a sketch of the calibration unit assembled are shown in Figure 6. The two IR emitters are mounted in a lamp holder facing the golden plate diffuser, and directing the light to the center of the diffuser. These sources guarantee a wide spectral output with an emitted radiance that resembles the one of a black body working at brightness temperatures of about 800-1000K under the conditions of use. Since the sources' emission is featureless and does

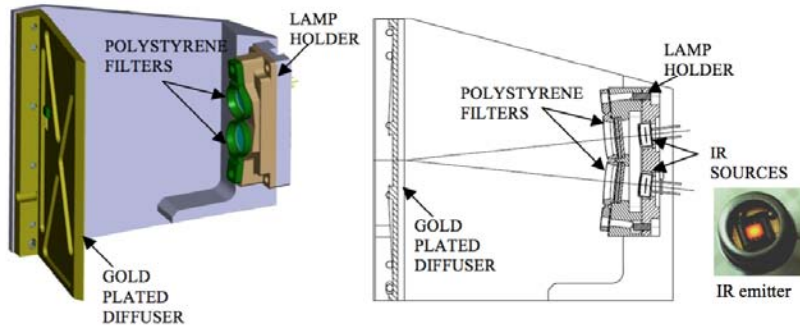


**Fig. 6** Calibration unit mounting. IR sources installed in the lamp holder with the polystyrene filters along the optical path. The light of the IR sources is scattered by the gold plated diffuser in the pupil of JIRAM detectors.

not contains any significant spectral features, a polystyrene filter has been placed in front of the sources in order to use its absorption bands as reference for spectral internal calibrations. The polystyrene spectral transmittance in the  $2\text{--}5\ \mu\text{m}$  range is characterized by weak absorptions around  $2.5\ \mu\text{m}$  and strong absorbing features at  $3.25$ ,  $3.26$ ,  $3.3$ ,  $3.4$  and  $3.5\ \mu\text{m}$  (stretching by aromatic-aliphatic group). The spectral transmittance of the polystyrene filter is depicted in Figure 5.

Finally, the golden plate diffuser has a rough surface optimized for the scatter-

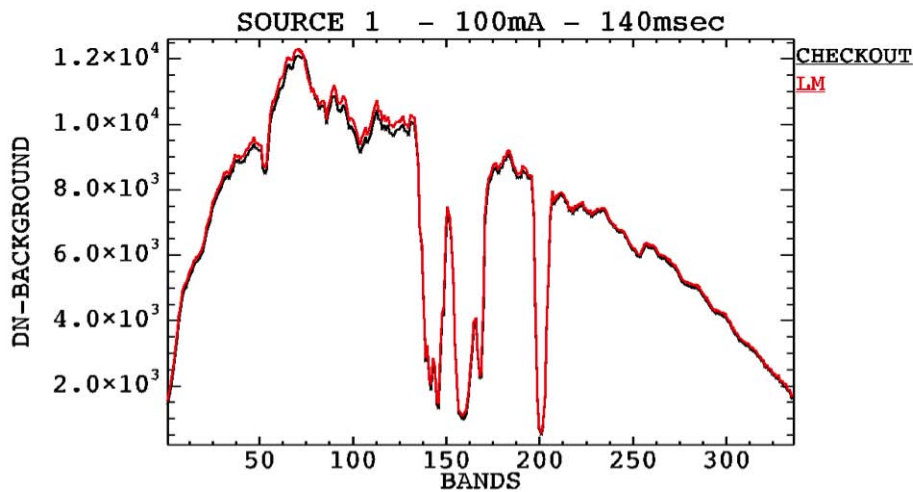


**Fig. 7** Spectrometer signal of the internal calibration source 1 driven at  $100\text{ mA}$  with an exposure time of  $140\text{ ms}$ . The red line represents the signal acquired during the on-ground test preformed at Lockheed Martin on March 2011. The black line represents the signal acquired during the first in-flight check-out after the launch on September 2011.

ing in the IR wavelength range. The reflectance of the diffuser is maximized at an angle of  $10\ deg$  w.r.t. normal direction. In this way the illumination of the optical paths is maximized for the chosen optical layout (see Figure 5). The two sources have been calibrated on ground. During these tests two working currents ( $75$  and  $100\ mA$ ) have been selected for the internal calibration procedure to be used in the flight operations. Figure 7 shows the measurements of the same calibration source acquired previously during the on ground calibrations and later during the first in-flight calibration of the instrument on September 3, 2011.

## 4 Instrument Calibration

### 4.1 Laboratory setup for pre-launch characterizations.

For the JIRAM experiment we foresee four broad calibration activities: spectral, geometrical, flat-field and radiometric. These measurements were completed during pre-launch tests in order to characterize the instrument responses.

The laboratory setup we used to characterize the spectral and geometrical performances of the spectrometer (SPE) and imager (IMG) channels is based on the same concept previously developed for similar imaging spectrometers like Rosetta/VIRTIS-M [Filacchione et al. (2006), Filacchione (2006), Ammannito et al. (2006), De Sanctis et al. (2011)]. The basic configuration consists of:

- JIRAM optical head, housed inside a thermo-vacuum chamber (TVC) to maintain operative temperatures (focal planes at  $80K$ ; instrument's optical bench at  $120K$ ).
- Data Processing Unit (DPU), housed inside TVC and connected to the optical head.
- EGSE (Electrical Ground Support Equipment) with a dedicated Master PC, electrically connected to the DPU.
- Optical bench equipped with an off-axis collimator aligned to the instrument boresight; several different targets and sources can be used at the collimator's focus according to the calibration requirements.
- OCS (Optical Control System) with relative Slave PC, electrically connected to the optical bench actuators (folding mirror) and equipment (reference lamps, monochromator, blackbody).
- Power supply.
- Data Archive/Post processing PC.

The setup configuration is summarized in Figure 8. The optical bench houses an off-axis collimator, a target holder placed at its focal plane and a folding mirror necessary to move the collimated beam in the JIRAM field of view. The folding mirror can be moved along both azimuthal and zenithal directions. The collimator's off axis parabola has a  $D = 250mm$  diameter, a  $F = 1020\ mm$  focal length and an off-axis angle of  $8\ deg$  which guarantees an unobstructed



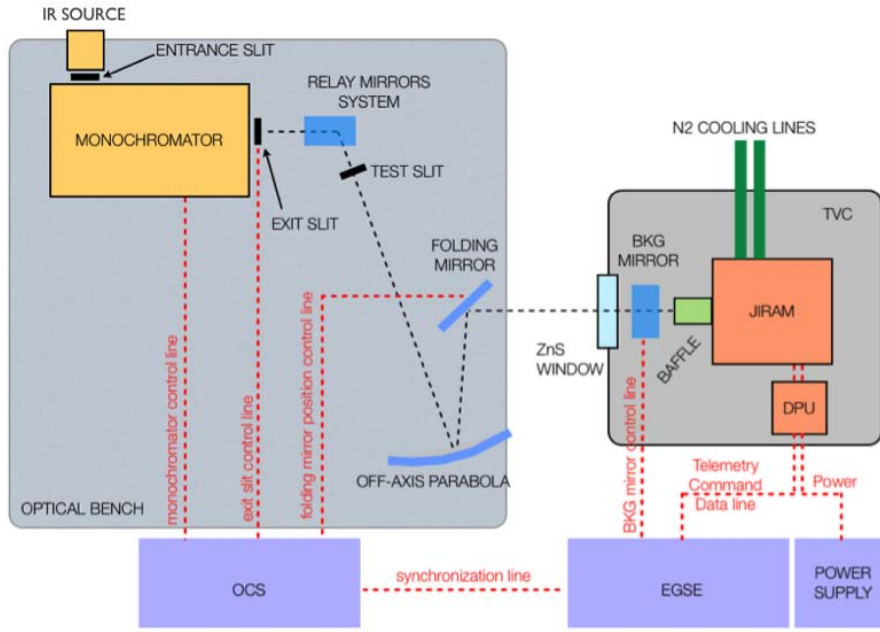


**Fig. 8** Block diagram of the calibration setup used to characterize the spectral and geometrical responses of JIRAM during on-ground tests. Facility property and engineering by Selex ES (Campi Bisenzio, Italy).

beam, reduced aberrations and a high magnification ratio; assuming a magnification ratio of  $F(JIRAM)/F(collimator) = 152/1020 = 0.149$  we have that  $1\text{ mm}$  on the collimator's focal plane shall correspond to  $0.149\text{ mm}$  on the JIRAM focal planes or  $3.725\text{ pixels}$  ( $40\text{ }\mu\text{m}$  pixel pitch). The target holder can house several interchangeable targets: pinholes, test slits, IR emitters geometrical pattern. In order to reproduce the operative conditions aboard the spacecraft, the instrument is housed in a thermo-vacuum chamber coupled to a thermal control interface (liquid nitrogen cooling line and thermistors). In this way it is possible to reproduce a vacuum environment at about  $10^{-7}\text{ mbar}$  and to cool down the optical head structure to about  $135\text{ K}$  and the two focal planes up to the operative temperature of about  $80\text{ K}$ .

The optical beam of the collimator reaches the pupil of the spectrometer, thanks to a ZnS window housed in front of the thermo-vacuum chamber. This window has an elevated optical transmittance in the  $25\text{ }\mu\text{m}$  range. A background mirror is placed on a two-position mechanism between the TVC window and the entrance baffle. This mirror is folded out of the instrument field of view during the acquisitions but can be commanded to a  $45\text{ deg}$  position respect to the boresight axis in order to point the TVC internal shroud. This configuration is particularly useful because it allows us to have a reference cold target (at about  $80\text{ K}$ ) over the background.



Two control systems are used in parallel during the measurements: the Optical Control System (OCS) is a dedicated slave setup capable of controlling the optomechanical devices (folding mirror, monochromator, sources) placed on the optical bench and of acquiring the corresponding telemetry data packets; the Electrical Ground Support Equipment (EGSE) is the master system from which we can command JIRAM acquisitions through the delivery of remote commands to the DPU. This system is capable of visualizing and saving the JIRAM data and the telemetry packets; the system starts the acquisitions when all optical elements commanded by OCS have reached the proper configuration for the measurement.

#### 4.2 Spectrometer: Spectral Calibration

*Spectral calibration at slit's center ( $FOVz = 0 \text{ deg}$ ).* The goal of the spectral calibration is to measure the wavelengths and spectral bandpasses sensed by the detector's pixels along the spectral dispersion axis. In a Littrow spectrometer the incident ( $\alpha$ ) and diffracted ( $\beta$ ) rays are in autocollimation ( $\alpha = \beta$ ) thus they are propagating along the same direction. In this case the grating's equation depends from the blazing angle wavelength  $\lambda_B$ :

$$\sin \alpha + \sin \beta = kn\lambda_B \quad (1)$$

where  $k$  is the diffraction order and  $n$  is the grooves density profile. Assuming a linear dispersion of the light along the spectral direction, it is possible to characterize the instrument by measuring the response of the pixels when they are sampled with a monochromatic light. Thanks to the spectral calibration measurements we can define for each pixel  $(m, n)$  - where  $m$  = frame sample (row) index and  $n$  = frame band (column) index:

- Spectral range: is the interval of wavelengths at which the instrument is sensitive;
- Sample Central Wavelength:  $\lambda(m, n)$  is the wavelength of the centroid of the Spectral Response Function measured on pixel.
- Spectral Sampling Interval:  $SSI(m, n)$  is the difference between two sample central wavelengths measured on each frame pixel.
- Spectral Width:  $SW(m, n)$  is the Full-Width-at Half-Maximum of the Spectral Response Function for each frame pixel.

As the instrument uses a diffraction grating that disperses the light according to a linear law we can assume  $SSI(n) = SSI$ . In this case the spectral calibration relation assumes the following expression:

$$\lambda_c(n) = \lambda_0 + SSI \cdot n \quad (2)$$

where  $\lambda_0$  is the sample central wavelength measured on the first sensitive band on the frame while  $SSI$  is the average spectral sampling interval. Both these quantities are retrieved from several finer spectral scans. We have used

**Table 1** Monochromator scan parameters performed for the spectral calibration.

Central wavelength (nm)	Spectral range (nm)	nm/step	Nominal bandpass (nm)	FOVz (deg)
2000	1970 – 2030	2	0.5	0
2100	2070 – 2130	2	0.5	0, $\pm 1.5$
3000	2970 – 3030	2	1	0
3500	3470 – 3530	2	1	0, $\pm 1.5$
4000	3970 – 4030	2	1	0
4900	4870 – 4930	2	0.9	0, $\pm 1.5$
5000	4970 – 5030	2	0.9	0

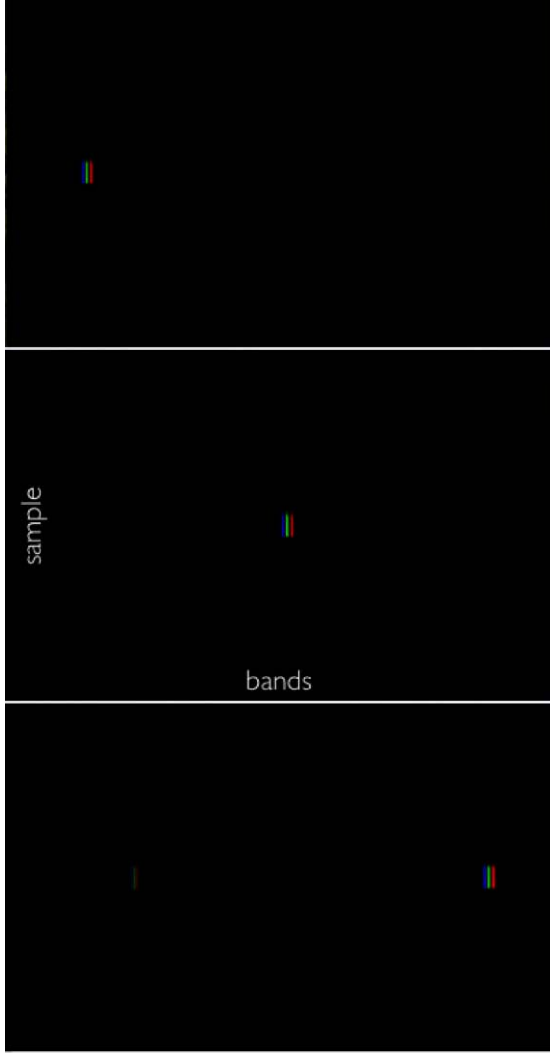
a monochromator (Princeton Instrument, model Acton SP2300) as source. JIRAM spectral response is sampled across different spectral ranges according to the parameters reported in Table 1. For each scan 31 steps are acquired in which the monochromator reference wavelength is moving at  $2 \text{ nm/step}$ . The measurement is repeated over three positions of the  $FOV$ , corresponding to the slit's center ( $FOVz = 0 \text{ deg}$ ), top ( $FOVz = 1.5 \text{ deg}$ ) and bottom side ( $FOVz = -1.5 \text{ deg}$ ). The slit image of the monochromator is about 10 samples wide along the JIRAM-SPE slit direction. Using such a configuration, we have acquired a temporal sequence of 31 acquisitions for each scan, where the temporal axis can be transformed in a spectral axis using the setting parameters of the monochromator; in this way it is possible to associate the wavelength of the input beam coming from the monochromator to each frame (see Figure 9). In the Figure 10, Figure 11 and Figure 12 we include the spectral profiles measured around  $2.1$ ,  $3.5$ ,  $4.9 \mu m$ ; such profiles are very uniform when measured across the samples illuminated by the monochromator: in fact profiles at samples 130, 135 and 140 are very similar in shape and width. Each acquisition is corrected for the background frame acquired by shutting off the monochromatic source. Background frames are collected with the same integration time of the measurements. The subtraction of the background frame is essential to improve the signal because it allows removing: 1) the focal plane's dark current generated by the spurious accumulation of thermal electrons; 2) the thermal emission generated by the instrument's internal walls and components; as the optical head is at operative temperature of  $120K$  while the focal plane is at about  $80K$ , this difference in temperature generates a signal increasing in the  $4\text{--}5 \mu m$  spectral range; 3) the thermal background induced by the thermo-vacuum window and by the external ambient (collimator and test slit). At each spectral profile we have applied a gaussian fit in order to measure the central wavelength, width and intensity of the signal. For brevity we include in Table 2, Table 3 and Table 4 the fitted parameters retrieved only from scans at  $2.1$ ,  $3.5$ ,  $4.9 \mu m$  and for samples 130, 135, 140 (similar data are retrieved for each scan reported in Table 1 for samples 130 to 140). The results of these gaussian fits are scattered on a JIRAM-SPE bands vs. monochromator's wavelengths plot. For each measurement we have included

**Table 2** Spectral calibration parameters retrieved from scan at 2100 nm. For brevity we include only the fit parameters corresponding to samples 130, 135 and 140.

Spectral scan at 2100 nm				
Sample	Band	Intensity (DN)	Center (nm)	FWHM (nm)
130	60	5909.0967	2081.6672	10.443477
135	60	6128.4062	2081.6836	10.370366
140	60	6535.5566	2081.5952	10.321414
130	61	6110.2344	2090.8320	10.576990
135	61	6403.8208	2090.7700	10.562078
140	61	6749.9575	2090.6997	10.543480
130	62	6281.7134	2099.8235	10.367974
135	62	6508.2148	2099.7957	10.344147
140	62	6900.1143	2099.7312	10.276349
130	63	6470.6943	2108.8875	10.579929
135	63	6683.7495	2108.8447	10.554585
140	63	7063.5723	2108.7856	10.504294
130	64	6836.9204	2117.9326	10.414031
135	64	7019.2676	2117.8914	10.513552
140	64	7495.0908	2117.8167	10.278224

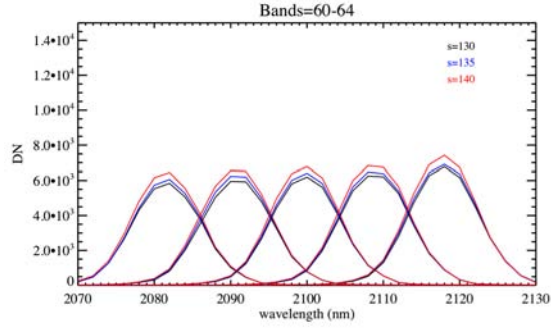
**Table 3** Spectral calibration parameters retrieved from scan at 3500 nm. For brevity we include only the fit parameters corresponding to samples 130, 135 and 140.

Spectral scan at 3500 nm				
Sample	Band	Intensity (DN)	Center (nm)	FWHM (nm)
130	215	8691.1396	3477.8677	12.444021
135	215	9142.2139	3477.8970	12.155180
140	215	9724.9961	3477.8279	11.942367
130	216	8481.0332	3486.9827	12.302603
135	216	8946.1143	3486.9714	12.094469
140	216	9651.6689	3486.9268	11.842725
130	217	8554.3838	3495.8635	12.597761
135	217	9143.5547	3495.9292	12.305345
140	217	9738.1660	3495.8809	12.072737
130	218	7940.5908	3504.9324	12.922405
135	218	9075.2812	3504.9248	12.430252
140	218	9738.4980	3504.8596	12.168459
130	219	8099.5000	3514.3789	12.190912
135	219	9209.4424	3513.9231	12.445724
140	219	9923.2676	3513.8494	12.146076
130	220	8681.3076	3523.0645	12.169569
135	220	9226.1221	3522.9775	12.096913
140	220	10008.612	3522.8972	11.891188

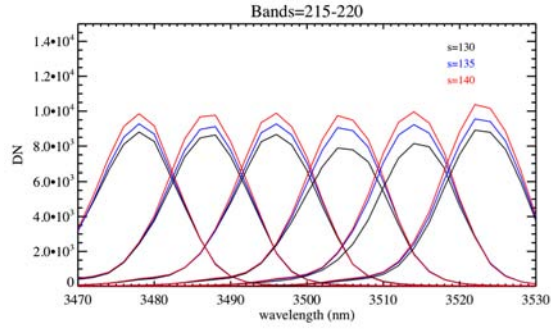


**Fig. 9** Monochromator's scan acquisition frames used for spectral calibration. Top panel: measurements around 2100  $nm$  composed as RGB image (B band: measurement at 2070  $nm$ ; G band at 2100  $nm$ ; R band at 2130  $nm$ ). Central panel: measurements around 3500  $nm$  composed as RGB image (B band: measurement at 3470  $nm$ ; G band at 3500  $nm$ ; R band at 3530  $nm$ ). Bottom panel: measurements around 4900  $nm$  composed as RGB image (B band: measurement at 4870  $nm$ ; G band at 4900  $nm$ ; R band at 4930  $nm$ ). The faint signal visible around 2450  $nm$  corresponds to the monochromator's 2<sup>nd</sup> diffraction order. The test slit illuminates about 10 pixels (samples 130 to 140).

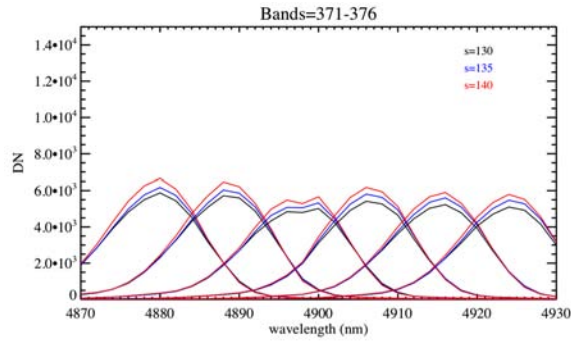
the error along the wavelength axis, which corresponds to the FWHM value. According to equation 2 the profiles centers must be aligned along a linear dispersion law (see Figure 13). After having applied a best linear fit to these points we obtain the calibration parameters to be used in equation 2, which are



**Fig. 10** Monochromator's scan profile around 2100 *nm*. Each profile corresponds to the scan acquired at samples=130,135,140.



**Fig. 11** Monochromator's scan profile around 3500 *nm*. Each profile corresponds to the scan acquired at samples=130,135,140.

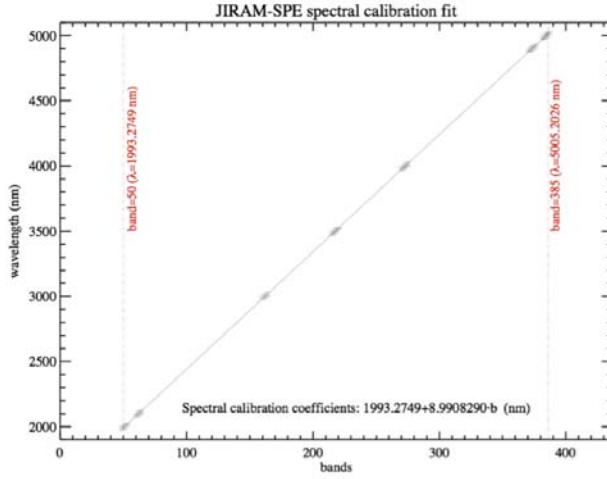


**Fig. 12** Monochromator's scan profile around 4900 *nm*. Each profile corresponds to the scan acquired at samples=130,135,140.

$\lambda_0 = 1993.2749 \text{ nm}$  and  $SSI = 8.9908290 \text{ nm/band}$ . Here  $\lambda_0$  is the intercept of the fitting line on the first useful band and  $SSI$  is the slope of the line. As mentioned before, JIRAM-SPE uses a focal plane wider with respect to the dispersion angle of the grating. For this reason it is necessary to resize it from

**Table 4** Spectral calibration parameters retrieved from scan at 4900 nm. For brevity we include only the fit parameters corresponding to samples 130, 135 and 140.

Spectral scan at 4900 nm					
Sample	Band	Intensity (DN)	Center (nm)	FWHM (nm)	
130	371	5819.1201	4879.4033	13.917690	
135	371	6106.7041	4879.4790	13.565055	
140	371	6569.9829	4879.3594	13.271798	
130	372	5569.3857	4888.2788	13.388824	
135	372	5847.5776	4888.3560	12.983862	
140	372	6252.0864	4888.2339	12.729793	
130	373	5048.5938	4897.3423	14.698156	
135	373	5355.8965	4897.3726	14.275899	
140	373	5690.0674	4897.2539	14.002407	
130	374	5395.9678	4906.2261	13.489372	
135	374	5783.0991	4906.2539	13.150321	
140	374	6141.9004	4906.1411	12.927224	
130	375	5245.9038	4914.9873	14.429183	
135	375	5579.6831	4915.0483	13.941272	
140	375	5867.9697	4914.9321	13.666830	
130	376	4820.1660	4923.9297	14.241017	
135	376	5162.1201	4923.9873	13.779602	
140	376	5456.6880	4923.8276	13.528606	

**Fig. 13** Spectral calibration parameters retrieved for JIRAM-SPE central samples ( $FOVz = 0 \text{ deg}$ ). The crosses correspond to the monochromator's spectral scans (centers and FWHMs) taken around 2000, 2100, 3000, 3500, 4000, 4900, 5000 nm. The best-fit line and parameters ( $\lambda_0$ , SSI) are indicated. The two vertical lines correspond to the spectral range extremes.

full frame (270 x 438 *pixels*) to effective frame (256 x 336 *samplexbands*). The resulting windowing is from 50 to 385 *bands*, which correspond to wavelengths  $\lambda_0 = 1993.2749 \text{ nm}$  to  $\lambda_{335} = 5005.2026 \text{ nm}$ ; these values correspond

to the JIRAM-SPE full spectral range. Along the spatial axis the windowing is performed from 12 to 267 *samples*.

*Spectral calibration at slit's edges ( $FOVz = \pm 1.5 \text{ deg}$ ).* . Being JIRAM-SPE an imaging spectrometer, we need to evaluate if there are any changes of the spectral response along the spatial direction (*samples*). For this reason we performed some additional scans with the monochromator at the two extremes of the  $FOVz$  ( $\pm 1.5 \text{ deg}$ , see Table 1).

The method explained in the previous paragraph was repeated in these two cases obtaining a spectral response similar to that measured at the slit's center ( $FOVz = 0 \text{ deg}$ ). In Figure 14 and Figure 15 we show the spectral fits

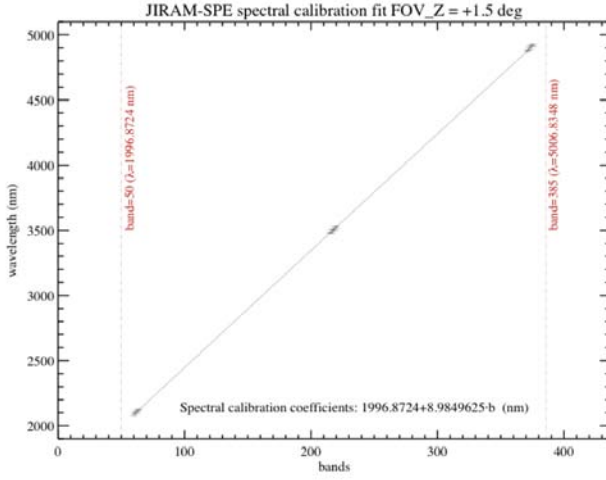


**Fig. 14** Spectral calibration parameters retrieved for JIRAM-SPE positive extreme samples ( $FOVz = +1.5 \text{ deg}$ ). The crosses correspond to the monochromator's spectral scans (centers and FWHMs) taken around 2100, 3500, 4900 *nm*. The best-fit line and parameters ( $\lambda_0$ , SSI) are indicated. The two vertical lines correspond to the spectral range extremes.

retrieved from  $FOVz = \pm 1.5 \text{ deg}$  scans.

By comparing the spectral calibration results at the three spatial positions of the  $FOVz = 0 \text{ deg}$  (sample=135),  $+1.5 \text{ deg}$  (sample=26),  $-1.5 \text{ deg}$  (sample=246) we can clearly verify that the instrument's response is homogeneous (see Figure 16). Hereafter sample and band positions will be indicated by *s* and *b* respectively for brevity. At  $3.5 \mu\text{m}$  a very small variation can be seen between the two extremes ( $3.52255 \mu\text{m}$  at *s*=26 and  $3.52365 \mu\text{m}$  at *s*=246) with respect to the slit's center ( $3.52257 \mu\text{m}$  at *s*=135). The situation is slightly worst at the two spectral extremes, where the slit's curvature introduces a maximum change of the response of about  $2.5 \text{ nm}$ . This is the case measured for *s*=135 (where  $\lambda = 4.92478 \mu\text{m}$ ) and *s*=26 ( $\lambda = 4.92723 \mu\text{m}$ ).

A measurement of the band cut-on and cut-off of the spectrometer and situation at the order sorting filters junction is plotted in Figure 17. Cut-on and

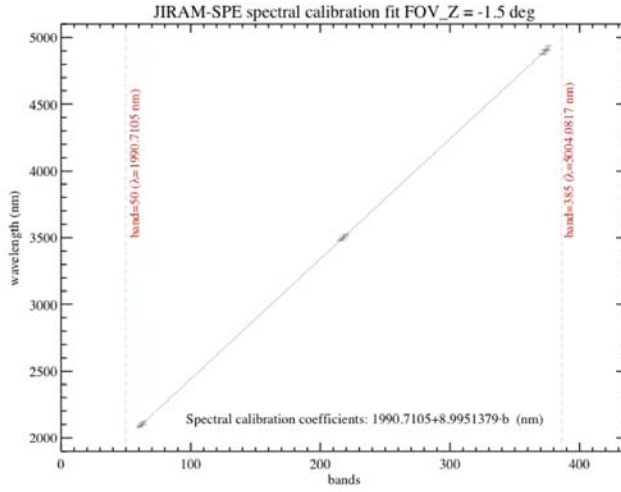


**Fig. 15** Spectral calibration parameters retrieved for JIRAM-SPE negative extreme samples ( $FOV_z = -1.5$  deg). The crosses correspond to the monochromator's spectral scans (centers and FWHMs) taken around 2100, 3500, 4900 nm. The best-fit line and parameters ( $\lambda_0$ , SSI) are indicated. The two vertical lines correspond to the spectral range extremes.

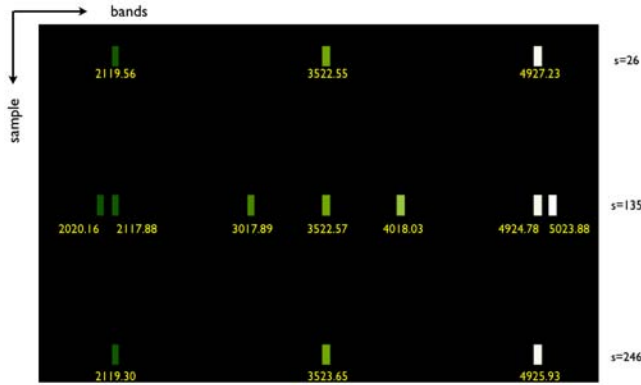


**Fig. 16** Variation of the spectral response on the JIRAM-SPE focal plane as measured on the three  $FOV_z$  positions (0 deg corresponds to sample=135; +1.5 deg is at sample=26; -1.5 deg at sample=246).

cut-off are given at the wavelengths where the efficiency of the detector is at 50% of the maximum in the filter's range. For the short wavelengths filter the cut-on and cut-off are respectively 2053 nm and 3762 nm. This filter reaches its maximum of transmission at 2190 nm. For the long wavelength filter the cut on and cut off are respectively at 3815 nm and 5040 nm and its maximum of transmittance is at 4816 nm.



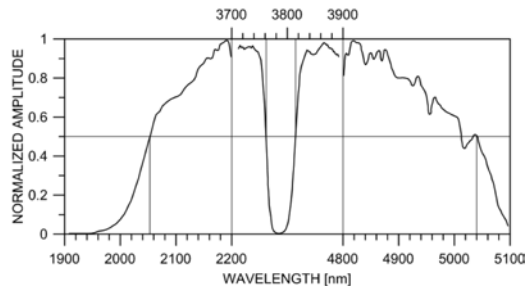


**Fig. 17** Normalized cut on and cut off of the spectrometer and situation at the junction of order suppressing filters.

#### 4.3 Spectrometer: Geometrical Calibration

Within the category of geometric calibration we include several measurements that allow us to define the pixel *IFOV* both along and across the direction of the slit, and the *FOV* of the instrument. In these cases we used an illuminated test slit placed at the focal plane of the collimator. The test slit has a width of about  $85\ \mu\text{m}$  that corresponds, through the magnification ratio of the setup, to about  $1/3$  of pixel ( $12\ \mu\text{m}$  or  $80\ \mu\text{rad}$ ) on JIRAM-SPE focal plane. The source we selected is the zero order light generated by the monochromator: in this case in fact we need a continuum source able to stimulate the instrument across the entire spectral range.

*IFOV along Y axis.* The measurement of the *IFOV* along Y-axis requests us to perform a spatial scan with the test slit oriented parallel to the JIRAM slit (Figure 18). The scan is done by moving the folding mirror (FM) of the optical

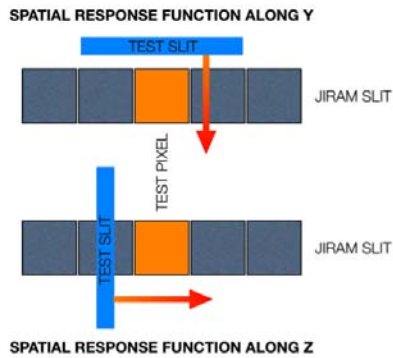


**Fig. 18** Measurement of the Spatial Response Functions along Y and Z. In the first case the test slit is oriented parallel to the JIRAM slit; in the second case it is perpendicular.

test bench for 81 times with a mechanical step of one tenth of a pixel. The

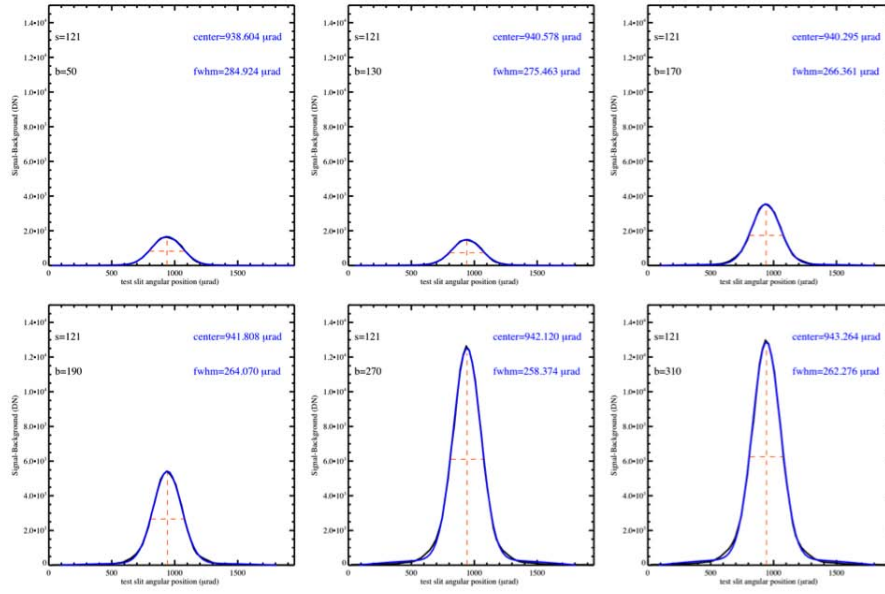


**Fig. 19** Spatial Response profiles (black curves) along Y and Gaussian fits (blue curves) measured at  $FOVz = 0 \text{ deg}$  (sample=121). From top left to bottom right scans taken at bands=50, 130, 170, 190, 270 and 330.

test slit is lighted by the zero order of the monochromator so that the signal is continuous but does not possess uniform intensity along the full spectral range. In particular JIRAM detect the strong telluric  $CO_2$  band that absorbs the signal in the  $4.26 \mu m$  range. The spatial scans are repeated three times at boresight ( $FOVz = 0^\circ$ ) and at two extremes of the field of view ( $FOVz = \pm 1.5^\circ$ ). Each acquisition is corrected for the background frame. After having considered the windowing of the focal plane, i.e. the sizing along  $b=50-386$  and  $s=13-268$ , the slit functions are measured in these intervals:  $s=1-16$  at  $FOVz = +1.5^\circ$ ;  $s=114-129$  at  $FOVz = 0^\circ$  and  $s=225-240$  at  $FOVz = -1.5^\circ$ . Once the test pixel is fixed at sample= $s$ , during the scan we measure a gaussian shaped profile as the signal increases, reaches a maximum and then decreases. This behavior is a consequence of the alignment of the test slit with respect to the JIRAM-SPE slit. The measured profiles and the gaussian fit profiles are shown in Figure 19, Figure 20, and Figure 21. The measurement of the spatial response function along Y gives us an estimate of the spatial resolving power of the instrument. The widths of the spatial response profiles show a small variation as a function of the wavelength. Since we have used a continuum light source (the zero order of the monochromator) we can measure the FWHM of the profiles for each wavelength. In Figure 22 we report the variation of the spatial responses widths along the entire JIRAM-SPE spectral range. For the three positions sampled, the maximum width is reached around band 25 while it decreases at higher bands. Around band 70 the profiles are affected by low

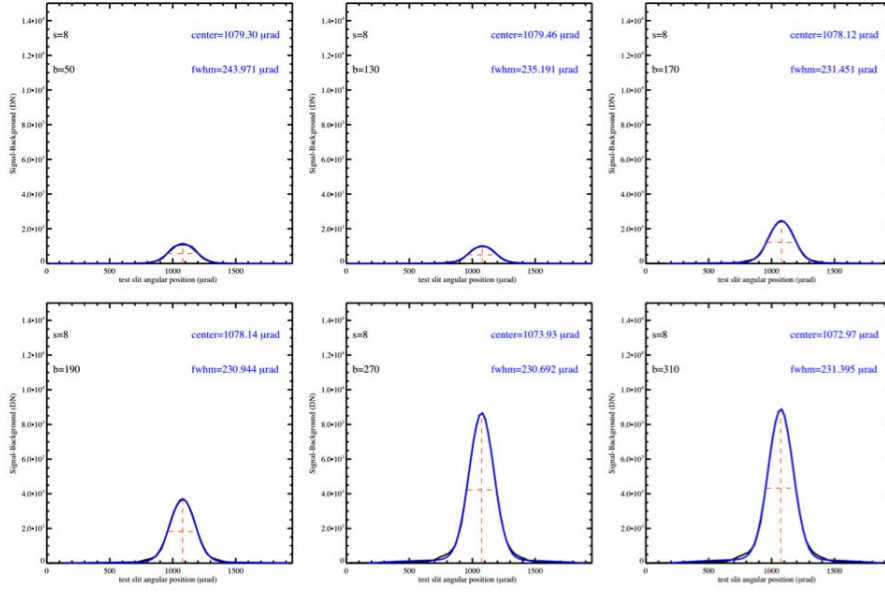


**Fig. 20** Spatial Response profiles (black curves) along Y and Gaussian fits (blue curves) measured at  $FOVs = 1.5 \text{ deg}$  (sample=8). From top left to bottom right scans taken at bands=50, 130, 170, 190, 270 and 330.

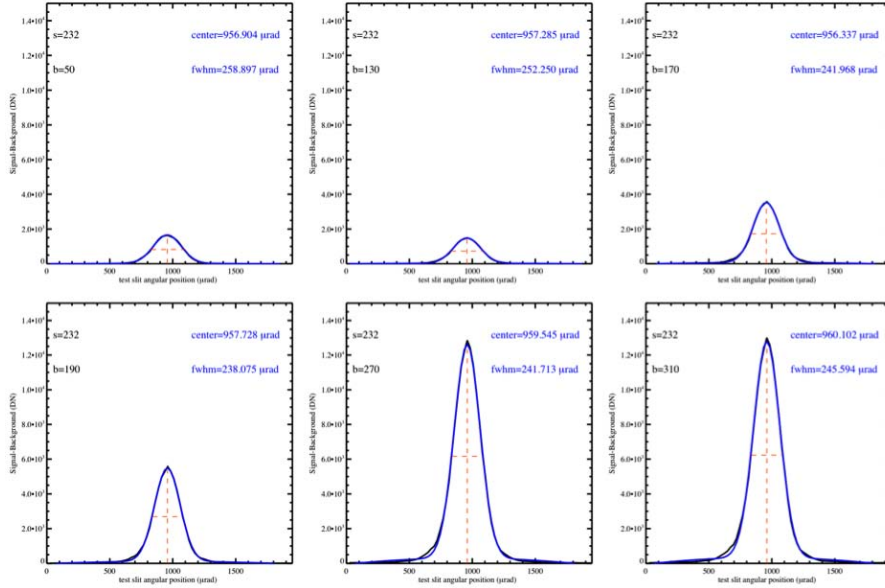


**Fig. 21** Spatial Response profiles (black curves) along Y and Gaussian fits (blue curves) measured at  $FOVs = -1.5 \text{ deg}$  (sample=232). From top left to bottom right scans taken at bands=50, 130, 170, 190, 270 and 330.

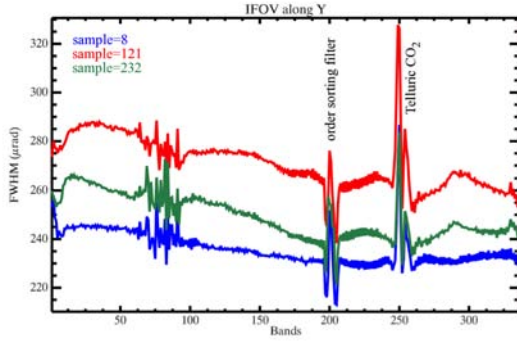


**Fig. 22** Spectral variation of the spatial response functions widths along Y axis. The three profiles correspond to the measurements done on three positions of the field of view, e.g. at samples 8, 121, 232. The three profiles are always well below the maximum acceptable level of  $360 \mu\text{rad}$  coming from 1.5 times the nominal *IFOV* ( $240 \mu\text{rad}$ ).

signal-to-noise conditions while the spikes observed around band 200 are due to the junction gap in the order-sorting filters. The  $4.26 \mu\text{m}$  range, around band 250 is strongly affected by telluric  $\text{CO}_2$  absorption band. From these results we can conclude that JIRAM-SPE spatial performances along the Y direction are very good, and satisfactory across the entire focal plane. There are two reasons for this: 1) the spatial profiles are gaussian and don't show any secondary peak or asymmetric shape respect to the center; 2) the *FWHM* are well-grouped below the acceptable limit of  $360 \mu\text{rad}$  resolution acceptable limit corresponding to 1.5 times the nominal *IFOV* ( $240 \mu\text{m}$ ).

*IFOV along Z axis.* The strategy to measure the *IFOV* along the Z-axis is similar to the previous one (see Figure 18, bottom panel). In this case the test slit placed at the collimator's focal plane has a width of 1/3 of pixel and is oriented perpendicular to the JIRAM-SPE slit. The scan is done by moving the FM for 81 times with a mechanical step of one tenth of a pixel. The test slit is illuminated by the monochromator's zero order thus the signal is continuous, but it lacks uniform intensity, along the full spectral range. Also in this case telluric  $\text{CO}_2$  absorbs the signal in the  $4.26 \mu\text{m}$  range.

Pixel function profiles are calculated for samples  $s=120-126$  by using a gaussian fit for each band. the spatial profiles and gaussian fit results taken at sample=124 are shown in Figure 23. The general trend corresponds to an angular shift of the gaussian peak positions of about  $200 \mu\text{rad}$  between the two spectral extremes ( $2.0$  and  $5.0 \mu\text{m}$ , see Figure 24).

This effect corresponds to a spectral tilt of less than 1 pixel on 336 bands and is probably due to a detector's mis-orientation with respect to the nominal spectral direction. We consider this behavior negligible and inside the instrument's mechanical tolerances.

Also the spatial performances along the Z direction are satisfactory because: 1) the spatial profiles are gaussian and don't show any secondary peak or

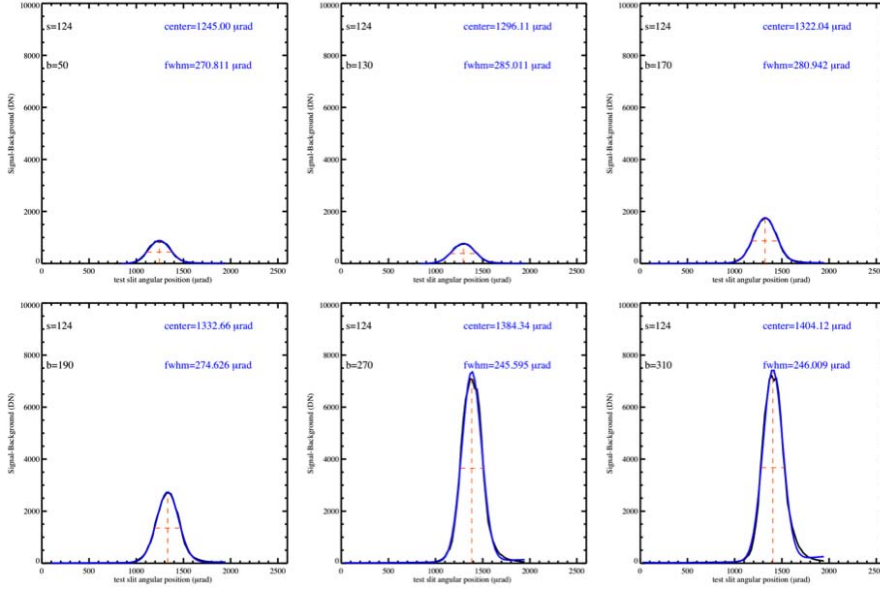


**Fig. 23** Spatial Response profiles (black curves) along Z and Gaussian fits (blue curves) measured at  $FOV_z = 0 \text{ deg}$  (sample=124). From top left to bottom right scans taken at bands=50, 130, 170, 190, 270 and 330.

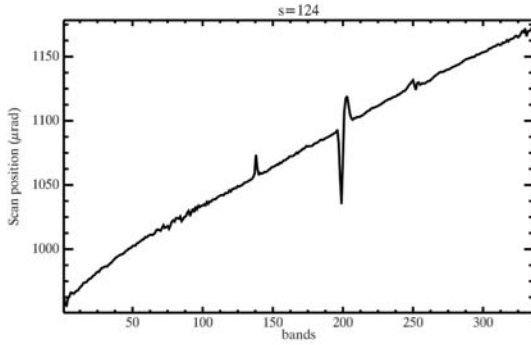


**Fig. 24** Variation of the peaks center positions along the spectral axis. An angular shift of the gaussian peak positions of about  $200 \mu\text{rad}$  between the two spectral extremes is detected.

asymmetric shape respect to the center (Figure 23); 2) the FWHM are always below the  $320 \mu\text{rad}$  resolution limit (Figure 25) corresponding to 1.5 times the nominal  $IFOV$  ( $240 \mu\text{m}$ ). The  $IFOV$  measurements were intensively repeated during the JIRAM integration to allow an optimal alignment of the telescope to the spectrometer and to reach the position of best focusing. This activity is complicated and time-consuming because the instrument is assembled and adjusted at ambient temperature while measurements are made at cryogenic conditions.

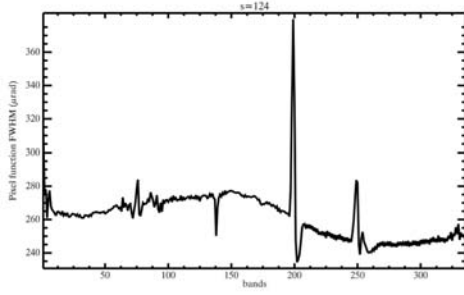


**Fig. 25** Spectral variation of the spatial response functions widths along Z axis sample=124. The profile is always well below the maximum acceptable level of  $320 \mu rad$  resulting from 1.5 times the nominal *IFOV* ( $240 \mu rad$ ). The order sorting filters junction gap is around band=200 while telluric  $CO_2$  introduces the spikes around  $b=250$ .

*FOV*. The last activity concerning the characterization of the geometrical performances of JIRAM-SPE is the measurement of the field of view. According to the requirements, the *FOV* of the spectrometer must be equal to  $3.52 \deg$  (being the width of the *FOV* equal to 256 samples of  $240 \mu rad$  each)  $\times 240 \mu rad$ . The measurement of the *FOV* is performed by using a 14 pinholes target placed at the collimator's focal plane. Each pinhole is illuminated by a small blackbody source (equal to the ones used as sources in the JIRAM internal calibration unit). The small pinholes are used in order to have point images on the JIRAM focal plane. Moreover these sources are placed at different heights respect to the housing plate because we want to reduce aberrations caused by the curved focal plane of the collimator's off-axis parabola. The sources indicated by numbers 9, 7, 3, 11 and 13 in the top-left panel of Figure 26 are aligned with respect to the JIRAM slit and then acquired. In this case we don't consider the remaining sources that will be used mainly to characterize the geometric response of the JIRAM-IMG channel. The resulting frame, corrected for the background, is shown in top-right panel of Figure 26. In this image, we can see that the 5 sources cover almost the full *FOV* with a sufficient signal across the full spectral range. The distribution of the sources is not equally spaced but has some asymmetries necessary to evaluate the top-bottom directions respect to the boresight. Thanks to a theodolite placed at the collimator's exit pupil (before the TVC entrance window), we have measured the zenithal angles of the sources respect to the horizontal plane ( $90^0 0' 0''$ ) obtaining the following values:

- Lamp#9:  $88^0 22' 59''$
- Lamp#7:  $89^0 01' 47''$
- Lamp#3:  $89^0 59' 09''$
- Lamp#11:  $90^0 47' 12''$
- Lamp#13:  $91^0 35' 30''$

The centers of the sources spots on the JIRAM frame (Figure 26 bottom panel) are placed at samples 250 (lamp#13), 203 (lamp#11), 133 (lamp#3),

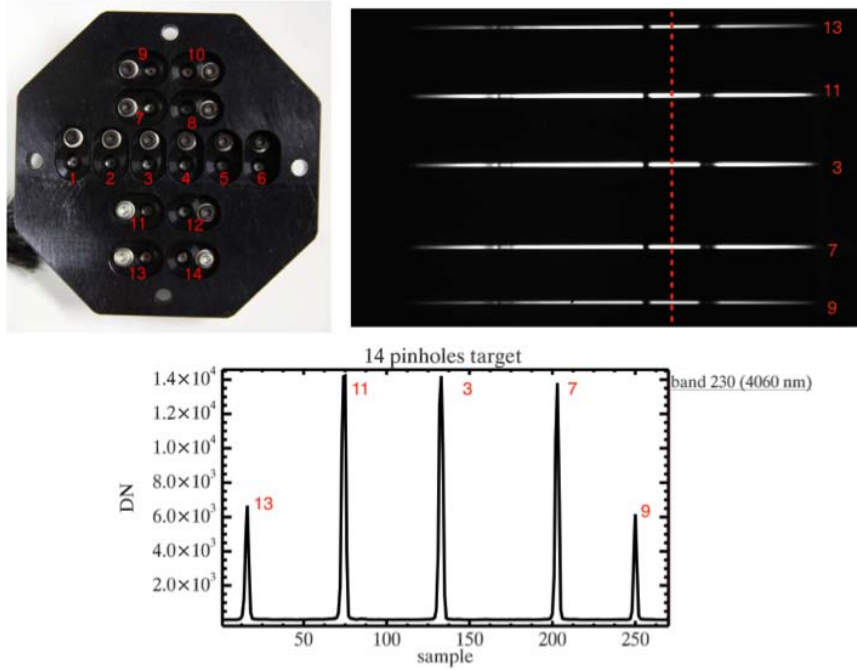


**Fig. 26** Top right panel: image of the 14 pinholes IR sources used to characterize the JIRAM *FOV*. For each lamp is indicated the identification number. The vertical line from lamp#9 to #13 is imaged through JIRAM slit giving the frame shown in the top left panel (bands axis along X and samples axis along Y). The lamps signals have a good signal across the full spectral range (order sorting filter junction gap is at band=200 and telluric  $CO_2$  at  $b=250$ ). The lamps positions are measured at band=230 (or 4060 nm) corresponding to the vertical red line on the frame. The resulting profile is shown in the bottom panel.

74 (lamp#7) and 16 (lamp#9). The distance between the two more external lamps (#13 and #9) corresponds to an angle of 3.2075 deg or 233.28 samples (240  $\mu rad$  each) while we measure a distance of 233 samples on the frame. Similar good matches are found between the different couples of sources and center positions measured on JIRAM frame. These results confirm that the instrumental *IFOV* and *FOV* values correspond to the requirements.

#### 4.4 Spectrometer: Flat-Field and Radiometric Calibration

In this section flat-field and radiometric calibration measurements are described. Flat-field is necessary to characterize the uniformity of the instrument response using a spatially uniform source [Filacchione et al. (2006), Filacchione (2006)]. In the case of imaging spectrometers using 2D detectors, like JIRAM-SPE, the flat field array contains, for each wavelength, the relative variation of the instrumental response with respect to the boresight (sample  $s^* = 128$ ).

**Table 5** Blackbody characteristics and performances.

Blackbody source	SBIR 2106 Model, Extended Temperature Differential Blackbody
Standard Temperature Range	$-20^{\circ}C$ to $+150^{\circ}C$ delta T (5C to 180C Absolute)
Emissivity	$0.985 \pm 0.015$ from $2 \mu m$ to $14 \mu m$
Temperature Measurement Accuracy	$\pm 0.1\%$ or $0.01^{\circ}C$
Stability	From $0^{\circ}C$ to $100^{\circ}C$ : $\pm 0.004^{\circ}C$ short term, $\pm 0.01^{\circ}C$ long term for $T > 175^{\circ}C$ : $\pm 0.025^{\circ}C$ short term, $\pm 0.04^{\circ}C$ long term

Flat field measurements were done during the prelaunch tests by acquiring the emitting area of a black body (see Table 5 for details) placed on the JIRAM optical pupil and aligned to the instrument boresight. In order to minimize the effects of telluric absorptions ( $CO_2$ ,  $H_2O$  vapor) the blackbody is housed in a chamber fixed to the TVC entrance window and continuously purged with a LN2 line during the measurements. The blackbody emitting area is sufficiently large to completely fill JIRAM *FOV*. Measurements were repeated with very different BB temperatures ( $10^{\circ}C$ ,  $25^{\circ}C$ ,  $50^{\circ}C$ ,  $75^{\circ}C$ ,  $100^{\circ}C$ ,  $125^{\circ}C$ ,  $150^{\circ}C$ ,  $175^{\circ}C$ ) and instrumental integration times (0, 20, 40, 60, 80, 100, 120, 140, 160, 180, 200, 400, 600, 1000 *ms*) in order to reach an optimal signal-to-noise ratio across the entire 2-5  $\mu m$  spectral range. The resulting flat-field array (*FF*) is given by the ratio of the signal measured at a certain position of the focal plane (*b*, *s*) with respect to the signal measured ad boresight ( $s^* = 128$ ) and at the same band position *b*:

$$FF(b, s) = \frac{DN(b, s)}{DN(b, s^*)} \quad (3)$$

The JIRAM flat-field array image (Figure 27) ranges between min = 0.019072 and max = 1.175823 with a mean = 0.968443 and a stdev = 0.068991. Flat-field allows to track detector's spatial variations (single and clusters of defective pixels, dis-uniformities caused by the production processes) and of the optical layout (the vertical feature around  $b = 200$  is caused by the order sorting filters junctions). The same setup used to characterize the flat field is used to retrieve the instrumental responsivity *R* (in  $DN \cdot m^2 \cdot \mu m \cdot sr \cdot W^{-1} \cdot s^{-1}$  units) thanks to the equation:

$$R(b, s^*) = \frac{DN(b, s^*, T)}{BB(b, T) \cdot \epsilon \cdot \tau_w \cdot t_{exp}} \quad (4)$$

where  $DN(b, s^*, T)$  is the signal (corrected for dark and background) measured on band *b*, sample  $s^* = 128$  with a *BB* temperature *T*;  $BB(b, T)$  is the spectral radiance emitted by the blackbody at temperature *T*,  $\epsilon$  the blackbody emissivity,  $\tau_w$  is the transmittance of the thermo-vacuum chamber window and  $t_{exp}$  is the instrumental integration time in seconds. The responsivity is



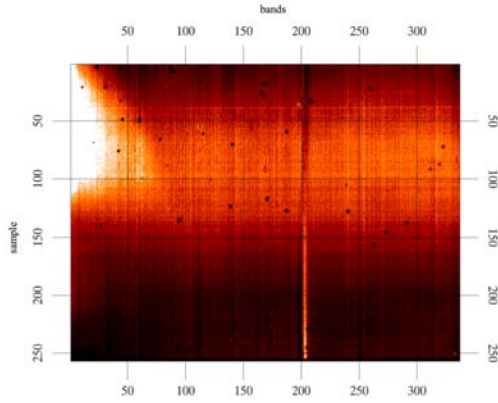


**Fig. 27** JIRAM-SPE flat field image. Dark spots correspond to defective pixels clusters. The vertical structure at about  $b = 200$  is caused by the order

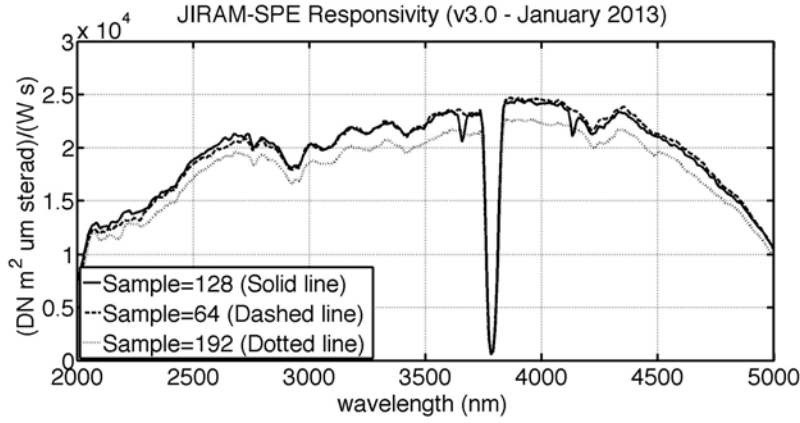


**Fig. 28** JIRAM-SPE responsivity profiles for samples  $s = 64, 128, 192$ .

measured across the entire  $2\text{--}5\ \mu\text{m}$  spectral range using the following combination of blackbody temperatures and integration times which guarantee the best signal-to-noise conditions:

- $2.0 < \lambda < 2.45\ \mu\text{m}$ : Blackbody  $T = 175^\circ\text{C}$ , integration time  $t_{exp} = 140\text{ms}$
- $2.45 < \lambda < 3.0\ \mu\text{m}$ : Blackbody  $T = 150^\circ\text{C}$ , integration time  $t_{exp} = 80\text{ms}$
- $3.0 < \lambda < 3.75\ \mu\text{m}$ : Blackbody  $T = 100^\circ\text{C}$ , integration time  $t_{exp} = 100\text{ms}$
- $3.75 < \lambda < 5.0\ \mu\text{m}$ : Blackbody  $T = 50^\circ\text{C}$ , integration time  $t_{exp} = 120\text{ms}$

The resulting responsivity profile measured at samples  $s = 64, 128$  and  $192$  are shown in Figure 28. JIRAM responsivity has a minimum at  $2\ \mu\text{m}$  where reaches the value of about  $7.6 \cdot 10^3\ \text{DN} \cdot \text{m}^2 \cdot \mu\text{m} \cdot \text{sr} \cdot \text{W}^{-1} \cdot \text{s}^{-1}$  and a minimum at  $5\ \mu\text{m}$  where is about  $1 \cdot 10^4\ \text{DN} \cdot \text{m}^2 \cdot \mu\text{m} \cdot \text{sr} \cdot \text{W}^{-1} \cdot \text{s}^{-1}$ . In average, in the range between  $2.5\text{--}4.5\ \mu\text{m}$ , is between  $2$  and  $2.5 \cdot 10^4\ \text{DN} \cdot \text{m}^2 \cdot \mu\text{m} \cdot \text{sr} \cdot \text{W}^{-1} \cdot \text{s}^{-1}$ . The small feature seen at about  $4.2\ \mu\text{m}$  is probably a residual of telluric  $\text{CO}_2$ .

#### 4.5 Spectrometer: Calibration pipeline

JIRAM-SPE flight data will be processed using a dedicated calibration pipeline. The principal task of this pipeline is to convert raw signal data, expressed in  $DN/s$ , in physical units of spectral radiance, in  $W/(m^2 \cdot \mu m \cdot sr)$ . According to Filacchione (2006), the instrumental signal can be expressed as:

$$DN(\lambda, t_{exp}, T, k_y) = \eta(\lambda) \cdot k_y \cdot t_{exp} \cdot \theta^2 \cdot S(\lambda, T) \cdot \frac{\lambda}{h \cdot c} \cdot \delta\lambda \cdot \frac{\pi \cdot D^2}{4} \quad (5)$$

being  $\eta(\lambda)$  the global quantum efficiency of the instrument,  $k_y$  the spatial binning parameter,  $D$  the telescope's pupil diameter,  $\theta$  the  $FOV$ ,  $\delta\lambda$  the spectral sampling and  $t_{exp}$  the integration time of the observation.

The responsivity  $R$  includes all the instrument-depending terms shown in equation 5. As discussed in section 4.4, the responsivity is typically measured on the center of the  $FOV$  in correspondence of the spatial pixel (sample)  $s^* = 128$  for each band. At this point the Instrument Transfer Function,  $ITF(b, s)$  can be determined, allowing us to retrieve the response across the whole focal plane by applying the flat-field  $FF$  (eq. 3) to the responsivity  $R$  (eq. 4):

$$ITF(b, s) = FF(b, s) \cdot R(b, s^*) \quad (6)$$

Finally, the target's spectral radiance,  $S$ , in  $W/(m^2 \mu m sr)$ , measured at wavelength  $\lambda$  and spatial position  $s$  along the slit's direction, is equal to:

$$S(\lambda, s) = \frac{DN(b, s)}{ITF(b, s) \cdot t_{exp}} \quad (7)$$

The conversion from the instrumental bands to wavelengths, is done using the spectral calibration law (eq. 2) with parameters  $\lambda_0 = 1993.2749 \text{ nm}$  and  $SSI = 8.9908290 \text{ nm/band}$  for the slit's center; the correspondence between the spatial position of samples on the frame and the geometric position of the resulting target's image is possible thanks to the geometric calibration parameters discussed in section 4.3.

#### 4.6 Imager: Spectral Calibration

The imager focal plane (IMG) is divided in two parts defined by the presence of two different band-pass filters facing the detector. The two filters are separated by an opaque region of dimension equivalent to about 10 pixels in the mid region of the detector along the rows.

The aim of the IMG spectral calibration is defining the spectral range detected by each channel (filter L, centered at  $3455 \text{ nm}$  with a  $290 \text{ nm}$  bandwidth; filter M, centered at  $4780 \text{ nm}$  with a  $480 \text{ nm}$  bandwidth).

The monochromator (Princeton Instrument, model Acton SP2355) installed on the test bench has been used to perform a spectral scan in the two nominal spectral ranges of the interference filters.

A first spectral scan has been performed from  $4.5 \mu m$  and  $5.1 nm$  with a step of  $5 nm$ . The monochromator's slit image has been located on the center of row 152 of the JIRAM-IMG, related to the filter M area. The monochromator's slit image is about 15 samples wide along the JIRAM-IMG zenith direction. In the Figure 29 the acquisition of the monochromator's slit image

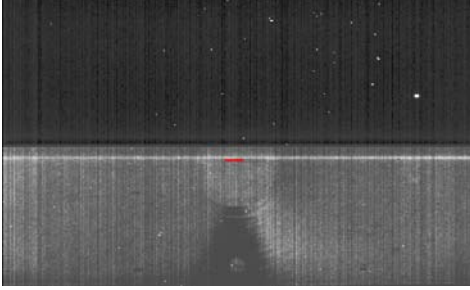


**Fig. 29** IMG acquisition of monochromator slit source at  $4800 nm$ . The position of the slit (red segment) is at the row 152 from column 208 to column 224 of the imager in the band M area.

at  $4.8 \mu m$  is depicted in red color. The 120 acquisitions has been performed every  $5 nm$ /step of the monochromator emission. The exposure time of the imager at each acquisition is of  $3 ms$ . The background data hve been removed from the signals. The average normalized signal of the slit image (row 152, column 208-224) is shown in Figure 30.

The spectral range detected by the IMG can be defined as the spectral range

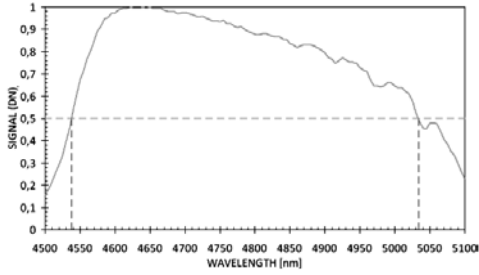


**Fig. 30** The average normalized signal of the slit image (row 152, column 208-224) in the band M (red line). The 50% of the maximum signal is depicted (horizontal dashed line), and the corresponding wavelengths of the spectral range are  $4537,5 nm$  and  $5035 nm$ .

corresponding to the signal range higher than 50% of the maximum. According to this definition the corresponding wavelengths of the spectral range are  $4537.5 nm$  and  $5035 nm$  and are depicted in Figure 30 related to the 50% of the maximum signal represented by the horizontal dashed line.

A similar process has been performed for the spectral characterization of L

band IMG: a spectral scan has been performed with the monochromator from  $3250\text{ nm}$  and  $3650\text{ nm}$  with a step of  $5\text{ nm}$ . The monochromator's slit image has been located on the center of row 118 of the JIRAM-IMG, related to the filter L area. In the Figure 31 the acquisition of the monochromator's slit im-

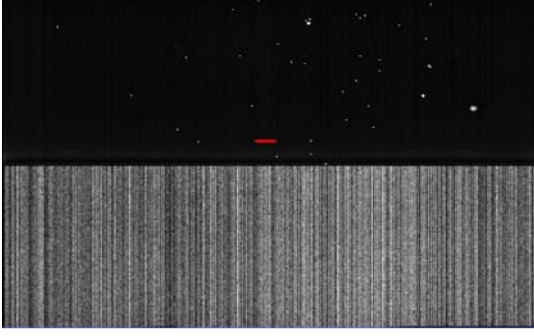


**Fig. 31** IMG acquisition of monochromator's slit source at  $3450\text{ nm}$ . The position of the slit is at the row 118 from column 208 to column 224 of the imager in the filter L area.

age at  $3450\text{ nm}$  is depicted in red color.

The 80 acquisitions have been performed every  $5\text{ nm/step}$  of the monochromator's emission. The exposure time of the imager was  $10\text{ ms}$  for every acquisition. The background data have been removed from the signals. The average normalized signal of the slit image (row 118, column 208-224) is shown in Figure 32 where a horizontal line indicates the 50% of the maximum signal. The

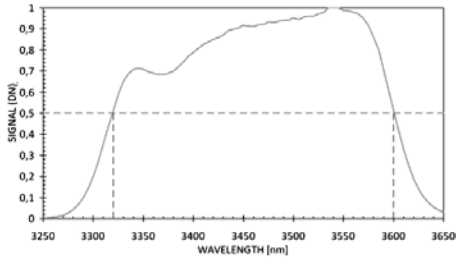


**Fig. 32** The average normalized signal of the slit image (row 118, column 208-224) in the band L (red line). The 50% of the maximum signal is depicted (horizontal dashed line), and the corresponding wavelengths of the spectral range are  $3320\text{ nm}$  and  $3600\text{ nm}$ .

corresponding wavelengths of the spectral range for the band L are  $3320\text{ nm}$  and  $3600\text{ nm}$ .

#### 4.7 Imager: Flat-Field Linearity and Radiometric Calibration

The IMG radiometric response of the imager for L and M bands has been obtained by acquiring the signal of the Black Body SBIR 2106 Model (Table 5) at different known temperatures and different exposure times. The Black Body was placed in front of the TVC where JIRAM was installed to fill the *FOV* of the IMG with a homogenous surface at the same temperature, as described in the previous sections on the spectrometer radiometric calibration. The responsivity of the IMG in each band is defined as:

$$R(\lambda_1, \lambda_2, T) = \frac{\int_{\lambda_1}^{\lambda_2} \epsilon \cdot RAD_{BB}(\lambda, T) \cdot \tau(\lambda) \cdot d\lambda}{\lambda_2 - \lambda_1} \quad (8)$$

where  $\lambda_1$  and  $\lambda_2$  are the wavelength limits of the spectral range for the band under calibration;  $\epsilon$  is the Black Body emissivity with a constant value of 0.985 in the IMG spectral range;  $RAD_{BB}(\lambda, T)$  is the spectral radiance of the Black Body at a given T temperature [ $W/m^2nm\text{sr}$ ];  $\tau(\lambda)$  is the measured transmittance of the ZnS window installed at the entrance of the TVC between JIRAM and the Black Body. The  $\tau(\lambda)$  behavior is shown in Figure 33.

A range of temperatures of the Black Body from  $0^\circ C$  to  $175^\circ C$  and different

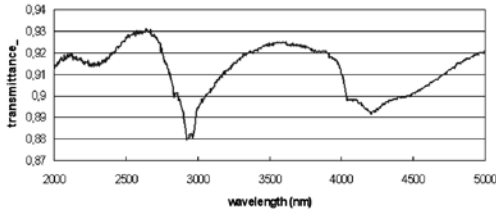


**Fig. 33** Transmittance of the ZnS window installed at the entrance of the Thermo Vacuum Chamber, between JIRAM and the Black Body.

exposure times of the IMG detector have been selected for different acquisitions. For both L and M bands, the exposure times have been selected in order to have a good linearity on the detector signal in the corresponding band. The instrument transfer function for the radiative calibration  $ITF_{RAD\_IMG}$  has been calculated from the equation:

$$ITF_{RAD\_IMG(\lambda_1, \lambda_2)} = \frac{DN(\lambda_1, \lambda_2, t_{exp}, T) - BG(\lambda_1, \lambda_2, t_{exp})}{t_{exp} \cdot R(\lambda_1, \lambda_2, t_{exp})} \quad (9)$$

where  $DN(\lambda_1, \lambda_2, t_{exp}, T)$  is the signal of the Black Body at temperature T acquired by the imager in the M or L band (at the corresponding spectral range  $\lambda_1, \lambda_2$ );  $t_{exp}$  is the exposure time of the acquisition which include the read time of 20 *nsec* that is the extra-period necessary for the acquisition of the electronic read out noise;  $BG(\lambda_1, \lambda_2, t_{exp})$  is the Back Ground signal acquired in the M or L band at the same exposure time, and  $R(\lambda_1, \lambda_2, t_{exp})$  is

the responsivity of the imager in M or L band at the Black Body temperature  $T$  as calculated from equation 8.

For the L band ( $\lambda_1 = 3320 \text{ nm}$ ,  $\lambda_2 = 3600 \text{ nm}$ ) radiometric responsivity a Black Body of  $150^\circ\text{C}$  temperature and an exposure time of  $1 \text{ ms}$  have been chosen. For M band ( $\lambda_1 = 4537.5 \text{ nm}$ ,  $\lambda_2 = 5035 \text{ nm}$ ) radiometric responsivity a Black Body of  $40^\circ\text{C}$  temperature and an exposure time of  $1 \text{ ms}$  have been chosen. The two acquisitions are shown in Figure 34.

The  $ITF_{RAD\_IMG}(\lambda_1, \lambda_2)$  of both bands in unit of  $DN/(s \cdot Wm^{-2}sr^{-1}nm^{-1})$

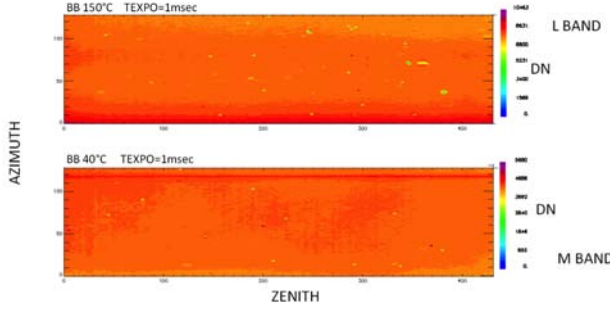


**Fig. 34** IMG acquisition with an exposure time of  $1 \text{ ms}$  of a Black Body with a temperature of  $150^\circ\text{C}$  top case L band and temperature of  $40^\circ\text{C}$  for bottom case M band.

is shown in Figure 35.

This instrument transfer function includes the flat-field matrix that represents

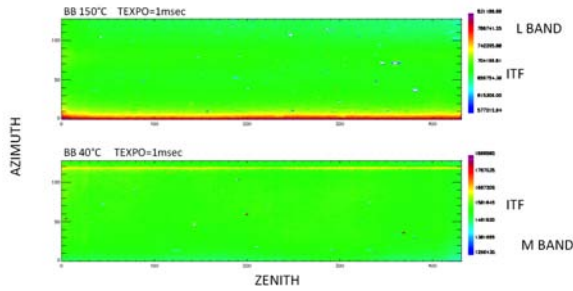


**Fig. 35** Instrument Transfer Function of the L band (top) and M band (bottom) imager.

the spatial variation of the signal acquired with the IMG detector of a spatially uniform target. From Figure 35 some variations on the signal along the detector can be noticed.

A more intense signal is evident at the bottom of the L band region, probably due to the effects of the photons coming through the M filter in the area close to the junction positioned between the M and L bands.

In the M band region a horizontal line of more intense signal can be observed,

possibly produced by the photons reflection on the junction surface separating the two filters.

The retrieved and calibrated signal in  $Wm^{-2}sr^{-1}nm^{-1}$  of another acquisition relative to Black Body temperatures of  $150^{\circ}C$  for the L band and  $40^{\circ}C$  for the M band is shown in Figure 36. As can be seen the retrieved signal shows

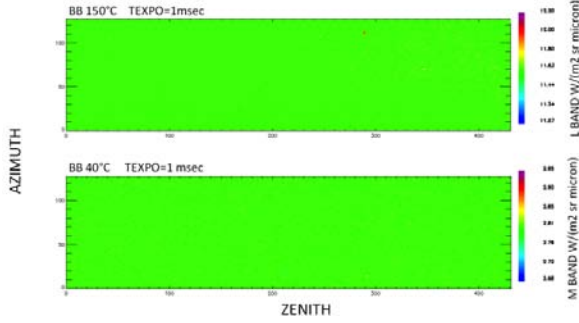


**Fig. 36** IMG L band (top) and M band (bottom) after radiometric and flat fiend correction.

a substantial homogeneity, except for some malfunctioning.

#### 4.8 Imager: Geometrical Calibration

The geometric calibration of the imager is carried out using the 14 pinholes target placed at the collimator's focal plane, as described in the previous sections for the geometric calibration of the spectrometer.

The position of each pinhole has been measured by means of a theodolite placed in front of the entrance of the TVC and reported in the table of the Figure 37, together with a picture of the 14 pinholes target. Each pinhole has been specified with a number. In correspondence of each pinhole 14 IF sources, similar to the couple of IR sources inside the calibration unit of JIRAM, are installed.

In the left panel of Figure 38 the acquisition with the IMG in the L band (top) and M band (bottom) of the 14 pinholes target is shown. The image of the 14 pinholes is well identified in the IMG yet without the subtraction of the background and the defective pixels. The pinholes number 9-7-3-11-13 are in correspondence of the spectrometer slit, row 152, represented by the red line in the M band. The relative acquisition with the SPE of the 5 pinholes aligned with the slit is shown in the right panel of Figure 38.

Comparing the distance between two pinholes target retrieved by means of the theodolite measurements with the correspondent distance in pixel between the centroid image of the two pinholes is possible carrying out the *IFOV* and *FOV* of the Imager.

To retrieve the *IFOV* the following pinholes have been considered: pinhole#4:

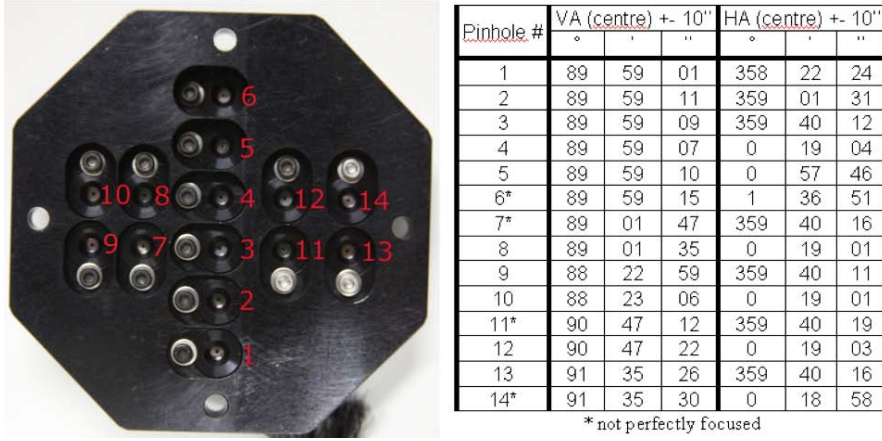


**Fig. 37** Image of the 14 pinholes target and corresponding table of the position carried out with the theodolite.

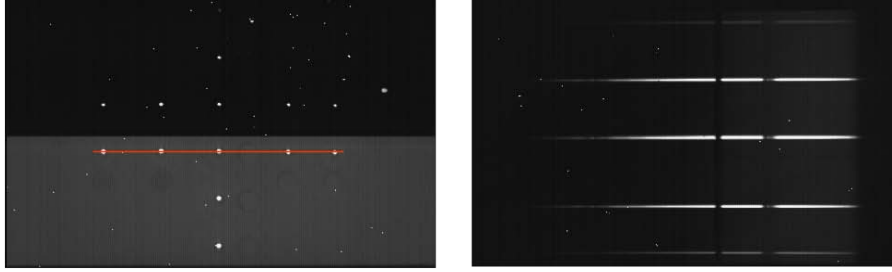


**Fig. 38** Left panel: acquisition with the IMG in the L band (top) and M band (bottom) of the 14 pinholes target. The image of the 14 pinholes is well depicted. The red line in the M band represents the position of the spectrometer slit in correspondence with the imager detector. 5 pinholes are aligned with the SPE slit. Right panel: acquisition with the SPE of the 5 pinholes aligned with the slit.

89°59'07'' and pinhole#12: 90°47'22'' for the along *Z* *IFOV*; pinhole#3: 359°40'12'' and pinhole#4: 0°19'04'' for the along *Y* *IFOV*. Considering the acquisition of the 14 pinholes target as reported in Figure 38 the corresponding position of the centroid image is for pinhole#4:  $y = 151.90$  and for pinhole#3:  $y = 104.41$  corresponding to  $IFOV = 246 \mu\text{rad}/\text{pixel}$  along *Y*; for pinhole#4:  $z = 217.14$  and for pinhole#12:  $z = 157.99$  corresponding to  $IFOV = 236 \text{ rad}/\text{pixel}$  along *Z*.

To retrieve the *FOV* the acquisition is carried out for different positions of the 14 pinholes target on the focal plane of the Imager. Using the folding mirror of the test bench, the image of the 14 pinholes target has been positioned translated respect the center of the IMG, in both directions *Y* and *Z*, in order to explore the geometric performance of the system. During the translation along *Z* of  $+1.3^\circ / -1.4^\circ$  the following pinholes have been considered: pinhole#10: 88°23'06'' and pinhole#14: 91°35'30''. Analyzing the position of the centroid



image of the 2 pinholes the *FOV* along Z of 5.9 *deg* has been carried out. During the translation along Y of  $+1.4^\circ / -1.7^\circ$  the following pinholes have been considered pinhole#3:  $359^\circ 40' 12''$  and pinhole#4:  $0^\circ 19' 04''$ . Analyzing the position of the centroid image of the 2 pinholes the *FOV* along Y of 3.76 *deg* has been carried out. These results confirm that the instrumental *IFOV* and *FOV* values correspond to the requirements.

#### 4.9 Imager: Calibration pipeline

The calibration pipeline of the imager is the procedure to convert raw data flight, expressed in  $[DN/s]$ , in the correspondent spectral radiance expressed in  $[Wm^{-2}sr^{-1}nm^1]$ . The generic acquisition in Digital Number (*DN*) of the IMG for L and M bands can be described by the equation [Filacchione (2006)]:

$$DN(\lambda_1, \lambda_2, t_{exp}, T, k_y) = \eta(\lambda_1, \lambda_2) \cdot k_y \cdot t_{exp} \cdot \theta^2 \cdot S(\lambda_1, \lambda_2, T) \cdot \frac{\Delta\lambda}{h \cdot c} \cdot \frac{\pi \cdot D^2}{4} \quad (10)$$

where  $\eta(\lambda_1, \lambda_2)$  is the global quantum efficiency of the instrument in the spectral range  $(\lambda_1, \lambda_2)$ ,  $k_y$  is the spatial binning parameter,  $t_{exp}$  is the exposure time of the observation,  $\theta$  is the *FOV*,  $S(\lambda_1, \lambda_2, T)$  is spectral radiance of the target at a given temperature  $T$ ,  $\Delta\lambda$  is the spectral range of the M or L band, and  $D$  is the telescope's pupil diameter. The target's spectral radiance  $S(\lambda_1, \lambda_2, T)$  in the equation 10, that will be acquired during the inflight JIRAM operations, can be expressed by the equation:

$$S(\lambda_1, \lambda_2, T) = \frac{DN(\lambda_1, \lambda_2, t_{exp}, T)}{t_{exp} \cdot ITF_{RAD\_IMG(\lambda_1, \lambda_2)}} \quad (11)$$

where  $\lambda_1$  and  $\lambda_2$  are the limits of the spectral range corresponding to the L band ( $\lambda_1 = 3320 \text{ nm}$ ,  $\lambda_2 = 3600 \text{ nm}$ ) or to the M band ( $\lambda_1 = 4537.5 \text{ nm}$ ,  $\lambda_2 = 5035 \text{ nm}$ ), as explained in section 4.7;  $DN(\lambda_1, \lambda_2, t_{exp}, T)$ ,  $t_{exp}$ ,  $BG(\lambda_1, \lambda_2, t_{exp})$  and  $ITF_{RAD\_IMG(\lambda_1, \lambda_2)}$  have been already defined in the same section in relationship to the equation 9 clarification.

#### 4.10 Instrument in-flight calibrations

The in-flight calibration is a standard procedure that provides a series of measurement to test the status of the instrument. From the operation point of view this procedure is identified with the label CAL among the standard JIRAM operation modes. The procedure can be launched at any the time in which it is needed and it is organized in 6 different steps. During the procedure the internal calibration sources are turned on in sequence and powered with two different reference currents. As the calibration unit is equipped by means of two sources they can be used alternatively or together according to the planning. Before and after the measurements with the calibration sources, some series of couples of background and detector read-out noise measurements are

performed. Each step is separated by a time longer than 30 s that is the interval between two spacecraft rotations. The internal calibration sources can be driven with different currents in the range between 75 and 100 mA. These values have been determined during the on-ground calibration tests for applying in the flight operations. Once the calibration source has been chosen, the internal calibration procedure is organized according to the following sequence: 1<sup>st</sup> step: acquisition of the background signal (the despinning mirror is pointing at the diffusive mirror of ICU).

2<sup>nd</sup> step: acquisition of the read out noise.

3<sup>rd</sup> step: acquisition of the source emission driven at 75 mA.

4<sup>th</sup> step: acquisition of the source emission driven at 100 mA.

5<sup>th</sup> step: second acquisition of the background signal.

6<sup>th</sup> step: second acquisitions of the read out noise. And so on.

The exposure times set during the calibration procedure are 6 ms for the imager and 140 ms for the spectrometer. Alternative calibration procedures can be operated with the second calibration source or by using both sources at the same time with half integration time both for imager and spectrometer. The read out noise is a characteristic of the detector and its value is depending on the construction characteristic of the focal plane. It appears as a systematic oscillation of the signal along the detector columns as shown in Figure 29 or Figure 31, where the raw data read from the IMG detector are reported. This kind of noise, besides a very small contribution depending on the detector temperature, is completely removed with the background. A read out noise estimation can be obtained by getting together focal plane information with a step of measurement acquisition, taken with an integration time virtually equal to zero (actually 20  $\mu$ s).

The red line depicted in Figure 7 is an example of the signal acquired by the spectrometer during the first instrumental turn-on after the launch. The red curve is the signal of the internal calibration test acquired during in-flight check out performed on September 2011 and has been obtained by using the calibration source labeled L1 and driven at 100 mA. The black curve represents the internal calibration relative to the acquisition that was carried out during the on-ground calibration test performed at the Lockheed Martin thermo-vacuum chamber facility on March 2011, before the launch. The signals are essentially the same and the features of the polystyrene are well reproduced, both that at 2.5  $\mu$ m and those between 3.2 and 3.5  $\mu$ m.

Observations of the Moon before the Earth closest encounter will be used to verify and refine the calibration done on the ground. This will permit to remove those possible systematic errors that can be introduced by the on ground test set up. The calibration facility on ground was certainly set to permit the instrument to operate with conditions that better replicate the flight ones. However the calibration set up cannot completely help reproduce the flight conditions and some residual errors can exist. A clear example is the JIRAM-SPE responsivity showed in Figure 28. The behavior of the curve in the range 2.0-2.4  $\mu$ m is expected to be different and dropping to lower values approaching the shorter wavelength towards 2.0  $\mu$ m. This error can be corrected by

using the Moon observations that can completely reproduce the observation geometries for which the instrument has been designed.

## 5 OPERATIONS

### 5.1 Planning and Commanding

The mission planning for the JIRAM experiment is driven by the goal of obtaining a maximum coverage over the planet. All periods of operations, when the spacecraft is closer in time less than -18 hours and +3 hours from the perijove, are considered data acquisition opportunities for JIRAM.

The major task of the Operation chain is the resolution of the overall mission conflicts, while facilitating and maximizing the science return. Spacecraft resources are shared among all the instruments on board the Juno spacecraft. Conflicts can arise either due to the spacecraft system or from Jupiter environmental constraints. System constraints arise from spacecraft pointing conflicts and the data volume limits. The data limit is compelled from the amount of memory allocated on the spacecraft for JIRAM or from the available downloadable data.

The JIRAM Operations Center (JOC), located in Rome, Italy, coordinates with the Juno Science Operations Center (JSOC) in SwRI, San Antonio TX, and with the Mission Operation System in JPL, Pasadena CA, to develop and update data taking plans as needed. It is necessary, during the mission planning phase, to accommodate the data observation strategies of all the instruments on the spacecraft. Inside the nominal operations, a long-term plan and the associated command sequences are established for data taking, timing and modes selection.

The aim of the planning and commanding activities is to give flexibility to the investigators in finalizing the science demands within the time frame given by the MOS (Mission Operation System) through the JSOC. The JIRAM mission planning is implemented via four plan levels as follows:

1. Generation of the Main Orbital Parameters;
2. Science Timeline Implementation Process;
3. Raw Commands Generation;
4. SASF (Spacecraft Activity Sequence File) Generation and Validation Process.

The first step of the Commanding Chain is the generation of the spacecraft orbital parameters, provided by the trajectory SPICE kernels (SPK) and handled by the JIRAM Geometrical Definition Tool (*JGeDeT*). The orbital parameters are stored into the JIRAM Local Archive to be available to the entire Commanding Chain. Figure 39 shows the main blocks for the management of the JIRAM Orbital Parameters. In particular the following steps are executed at every run of the *JGeDeT*:

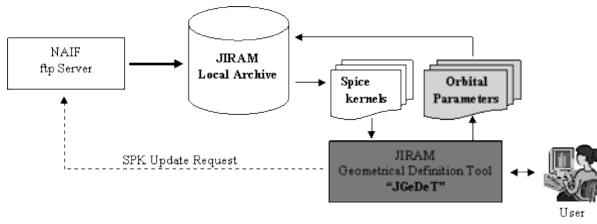


**Fig. 39** Flowchart of the JIRAM Geometrical Definition Tool.

1. Identification of the latest available Juno SPK products from the NAIF repository directory.
2. Update the SPK products into the JIRAM local archive.
3. Software Environment Configuration:
  - a. Selection of the orbits of interest;
  - b. Definition of the Orbit Sampling Factor.
4. Selection of the orbital parameters:
  - a. All available orbital parameters;
  - b. Limited class of orbital parameters.
5. Storage of the Orbital Parameters into the JIRAM Local Archive.
6. Graphical Visualization of the calculated orbital parameters.

The Science Timeline Implementation process culminates in the generation of the Science Activity Plan (SAP), implemented by Juno Science Operation Center (JSOC), and nominally contains the selection of science observation periods and the experiment's main science observation modes, imposed by mission conditions.

The main author of the Science Timeline Process is the JIRAM Planning Tool (*JPlaT*), necessary to support the JIRAM Science Community in the identification of the mission scientific objectives and then for the design of the operative timelines. The following steps characterizes the main utilities implemented in the JIRAM Planning Tool:

1. Identification of all the science areas interested by the selected flyby (orbit);
2. Prioritization of the science areas;
3. Analysis and validation of the achievable Science Goals, provided by the JIRAM Science Community, over the prioritized science targets;
4. Modeling of the Jupiter Radiation Environment for the identification of the No Working Regions.

A friendly translation of the SAP is the JIRAM Master Science Plan (*JMSP*) available to the JIRAM Science team through the JIRAM local archive. The *JMSP* nominally contains the selection of science observation periods in term of Scientific Operative Sequences imposed by the mission goals, mission conditions and constraints (time, data volume and power budget).

During the Commanding phase, the *JMSP* is refined in term of generation of the JIRAM Tele-Commands and parameters.

Accordingly to the JIRAM Raw Command Files (*JRCF*), generated by the

JIRAM Commanding Tool (*JCoT*), the raw sequences are then converted into the SASF format and finally checked and validated by the JIRAM Testing Tool before the official delivery to the DOM (Distributed Object Manager) client. Figure 40 shows the block diagram for the generation of the SAP and *JMSP*

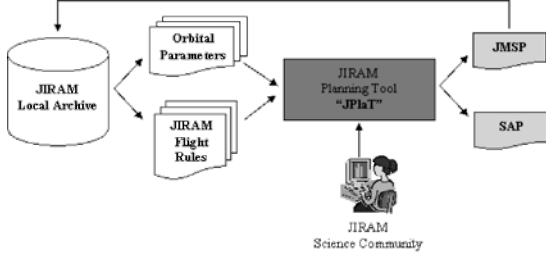


**Fig. 40** Flowchart of the JIRAM Planning Tool.

files. The orbital parameters and the Mission Flight Rules, are loaded into a temporary buffer of the *JPlat*. The inputs, provided by the JIRAM Science Community and ingested into the chain through a user-friendly user interface, complete the inputs of the internal science algorithms. Figure 41 is a graphical representation of the JIRAM Master Science Plan *JMSP*. At this stage of the Planning and Commanding process, only the science Blocks (Calibration and Science) are represented and entirely configured. During the Commanding phase, the *JMSP*/SAP product is refined in term of generation of the JIRAM Tele-Commands and parameters for the in flight hardware configuration, as schematically represented in Figure 42. The main Tasks executed by the JIRAM Commanding Tool (*JCoT*) can be described as following:

1. Selection of the Science Activity Plan (SAP) under consideration;
2. Check of the consistency between SAP and *JMSP*;
3. Definition of the Atomic Sequences in term of Tele-Commands and Settable Parameters;
4. Definition of the Timing (relative and absolute) and Duration of the Atomic blocks.

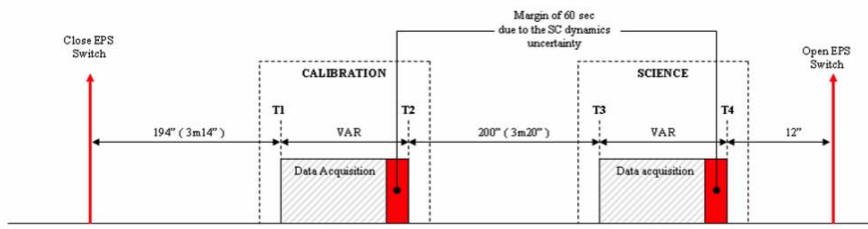


**Fig. 41** Graphical representation of the JIRAM Master Science Plan, *JMSP*. Timing and different work phases are depicted.

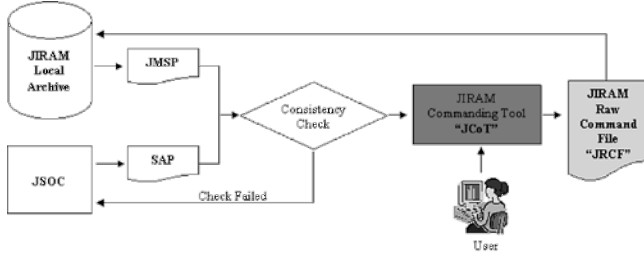


Fig. 42 Flowchart of the JIRAM Commanding Tool.

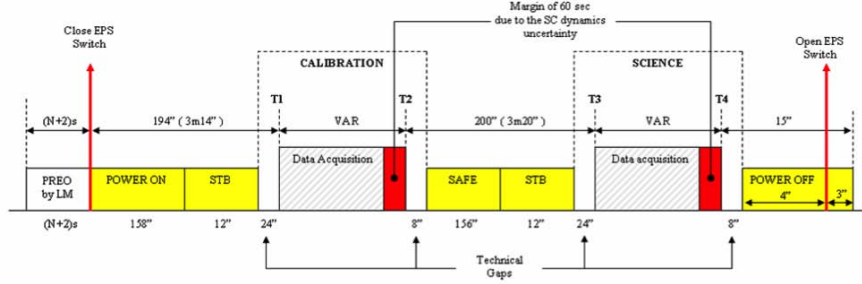


Fig. 43 Graphical representation of the JIRAM Raw Command File.

Figure 43 shows a graphical representation of the JIRAM Raw Command File. In yellow are highlighted the technical blocks inserted by the JIRAM Commanding Tool, to complete the timeline. Accordingly to the JIRAM Raw Command Files (*JRCF*), generated by the JIRAM Commanding Tool (*JCoT*), the raw sequences are then converted into SASF format and finally checked and validated by the JIRAM Testing Tool before the official delivery to the DOM client. The validation process implements the following activities on the SASF product:

1. Risk Parameters and Tele-Commands Identification (if any);
2. Calculation of the Power consumption and Data Volume Profiles;
3. Verification of the instrument Hardware Performances;
4. Verification of the instrument Science Performances;
5. Verification of the instrument Flight Rules;
6. Verification of the overall SASF timing;
7. SASF Syntax Checks;
8. Storage of the approved SASF file into the JIRAM local Archive;
9. Publish of the SASF file into the DOM server.

## 5.2 EGSE: capabilities and functionalities

The JIRAM EGSE (Electric Ground System Equipment) was designed to manage the instrument during all the testing and calibration phases before the

mission launch. The EGSE has been also designed for the JIRAM data management to retrieve and archive data during the data processing and analysis phase. In the present configuration, while equipped with additional hardware to interface during the test and calibration activity, the instrument consists of specialized software to assist in the data analysis. The EGSE permits the merging of original multiple data files downlinked from the spacecraft and the generation of a new global data archives from which data are lately reorganized and formatted according to the NASA PDS standard.

The new archives will be organized respecting their mode of transmission way from the instrument to the spacecraft, namely through the fast (HSSL) or the slow (LSSL) interface. The fast interface is the normal one and it has a redundancy. The slow interface is only used as back up if both the HSSL lines are interrupted.

EGSE performs a consistency check between the commanded sequence and the received telemetry from JIRAM. The telemetry and the telecommand (TM/TC) packets are identified and arranged by generation time and a log of the process is generated with the following information: name, number of packets, start time and stop time of the input archives.

### 5.3 Cruise testing and science activities

Test and measurements have been planned for the cruise to Jupiter. The planning has been done on the basis of the Juno project availability of resources and of the spacecraft orientation respect to the Sun. In fact the instrument is protected from the Sun illumination only when the spin axis of the spacecraft and the direction of the Sun form an angle lower than  $14^\circ$ . For larger angular values part of its optical head is illuminated and the temperature of the detectors increases proportionally with a consequent increase of the thermal noise. The condition improves with the increase of the distance from the Sun. Acceptable detector noise conditions for measurements are for temperatures below  $95K$ . Further decreases of the temperature reduce the detector thermal noise, improving the quality of the measurements. The reason for this condition is that the JIRAM position on the Juno aft deck is forced by the need for a proper unobstructed field of view in front of the instrument to avoid that unwanted stray light that could enter the instrument and contaminate the real measurements.

Most of the activities planned for the cruise are fundamentally oriented to the verification of the instrument conditions and some calibration activities. The verification of the instrument conditions is achieved by an internal calibration of the instrument according to the procedure previously described. The planned pointing calibrations are for the verification of the alignment of the JIRAM boresight with the spacecraft reference orientation and the alignment relative to other remote sensing instruments like the camera, JunoCam, and the UV spectrometer, UVS. During the Earth Flyby JIRAM will observe the Moon. This observation, besides being the only occasion during the cruise to

verify the execution of the science observing sequences as they will be operated at Jupiter, will be the occasion to verify, refine if needed, the radiometric calibration of the instrument. Science activity, in particular observation of the Galactic Center, is also planned during the cruise in November 2015 and February 2016, just before the arrival to Jupiter.

#### 5.4 Elements for the observation strategy at Jupiter.

The baseline for the JIRAM operations is during those orbits tagged as MWR, where the Juno's Microwave Radiometer is considered as prime instrument. During MWR orbits the spin axis of the spacecraft will be orthogonal to the orbit plane, then the Juno's orbit plane will pass through the center of the planet. Consequently, the JIRAM optical axis will be contained in the orbital plane and the instrument will have the most favorable view of the planet. Observation will be distributed in a time period between -18 hours and +6 hours from perijove. MWR orbits are the 3rd, 5th, 6th, and 7th orbits. The 8th orbit is also considered a MWR orbit but the spacecraft is going to be tilted to optimize the observing conditions of MWR. JIRAM could also operate during other orbits for a limited amount of hours around the perijove time. Such a limitation is due to the fact that the other orbits are planned for gravitational measurements that require a spacecraft orientation unfavorable to JIRAM. The main operations are planned to start a few hours after the spacecraft is turned in the MWR orbital position. That is, the observation time can start 18 hours before perijove time.

Observations will be normally extended for 3 hours after the perijove pass with the possibility of extending this time to 6 hours for a special auroral campaign in the southern hemisphere. During the observation period the spacecraft speed will be high and the spatial resolution at the planet (1-bar atmospheric level) will vary rapidly as a function of the distance of the spacecraft from the planet. The change of the pixel resolution during one of the MWR orbits is shown in Figure 44 during all the potential period of observation between -18 and +6

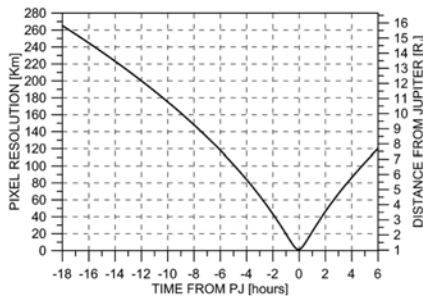


**Fig. 44** Pixel resolution at the planet 1-bar atmospheric level. The distance from the planet corresponding to the time from perijove is given on the right y-axis.



hours from perijove. The spatial resolution varies a lot with the time during the approach to the planet because of the fast motion of the spacecraft. It can range from about 260 km per pixel down to almost 1 km per pixel at the closet approach.

An important parameter to take into account planning the observations is the dwell time, namely the ratio between the instantaneous average size of the ground footprint and the modulus of the ground speed vector, which links the spatial resolution to the integration time. The JIRAM maximum allowed integration time is 1 s. The limit is imposed by the fact that Juno is a spinning spacecraft and the JIRAM's despinning mirror can only compensate for a limited time for mechanical reasons. Figure 45 shows the dwell time for the

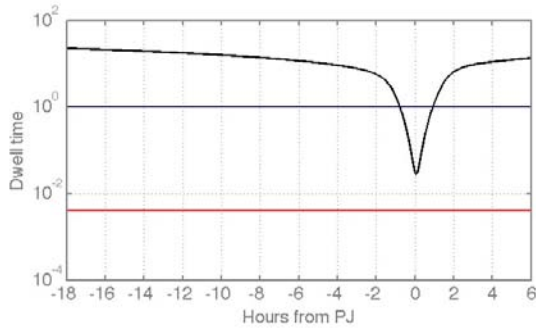


**Fig. 45** JIRAM dwell time. The red and the blue lines give the integration time range of variability between minimum and maximum respectively.

MWR orbits due to the motion of the spacecraft. The dwell time calculation considers the motion of spacecraft in respect to the Jupiter 1-bar surface and the the planet rotation. The horizontal lines show the minimum and the maximum integration times that JIRAM is going to use.

During each orbit, the quality of the measurements can be reduced by varying degrees by the presence of environmental radiation (energetic electrons and protons) present in Jupiter's magnetosphere. These energetic electrons and protons can penetrate the JIRAM instrument and create noise in the detectors. In general, protons generate larger noise signals in the JIRAM detectors, but they are significantly less abundant than energetic electrons which can reach very high fluxes. Electrons with energies higher than 10 MeV are expected to have fluxes that can range from  $10^2$  to  $10^7 \text{ e}^- \text{ cm}^{-2} \text{ s}^{-1}$ , depending on the position of the spacecraft on the orbit. The Divine/GIRE [Divine and Garrett (1983); Garrett et al. (2003), <http://www.openchannelfoundation.org/projects/GIRE/>] family of Jovian radiation models, as well as the 2005 update [Garrett et al. (2005)], are the basis of the estimates of the "raw" external Juno radiation environment used for our GEANT4-based JIRAM noise predictions.

An instrumental performance analysis has been carried out to define when and where, during the orbit, the observations can be done on the basis of the

type of observation to be planned. In fact, depending on the scientific objectives the types of measurement that JIRAM can provide are basically four and they are respectively auroral spectra, auroral images, atmospheric spectra, and atmospheric images. The signal from aurorae is normally low, then auroral observations, in particular the spectral measurements, require long integration times up to the limit of the JIRAM capability. This fact makes those observations at higher risk of contamination from environmental radiation. For other atmospheric observations no major problems would be encountered for images. There is more concern for the spectral measurements dealing with the retrieval of concentrations of minor atmospheric constituents like  $H_2O$ ,  $NH_3$  or  $PH_3$ , because electron noise can cause an increase of the error in the retrieval of the species abundances. Figure 46 shows the expected abundance of

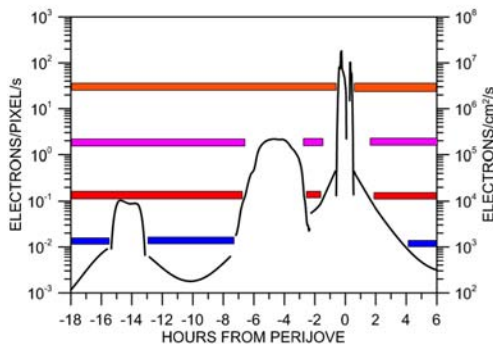


**Fig. 46** External 10-MeV integral electron flux for orbit 3. The colored bars give the periods of time in which different types of measurements can be done in the presence of the noise created by this radiation environment. In particular: blue, auroral spectra; red, auroral images; magenta, atmospheric spectra; orange, atmospheric images. This calculation is done for orbit 3 (proton noise events during these times have also been considered). The extension to +6 hours after perijove is also considered for a possible observational campaign on the southern hemisphere aurora.

environmental electrons with energies higher than 10 MeV at different times during the Juno approach to Jupiter. The color bars indicate the time when the different kinds of JIRAM observations are allowed. Such estimation has been done on the basis of the present knowledge of the radiation spectra in the Jovian magnetosphere which are derived from a combination of in-situ measurements from past Jovian missions, Earth based synchrotron emission observations, and model predictions. In those times the environmental condition can be considered acceptable although particular care has to be placed on the data analysis to remove the weight of the contaminated pixels.

Data compression can be applied to the data onboard the spacecraft. The aim of the compression is to reduce the data volume in order to be able to collect more images and spectra. Two different types of compression have been implemented in the flight software. They are differently specialized to work

**Table 6** JIRAM operational modes: data volumes without and with compression. Data volumes includes housekeeping and transmission protocol.

	frame size (pixels)	uncompressed data volume (Mbits)	compression factor	compressed data volume (Mbits)
<b>Imaging Modes</b>				
I0, No Imager	-	-	-	-
I1, Full Imager	256x432	1.8	6	0.3
I2, M-Band	128x432	0.9	6	0.15
I3, L-Band	128x432	0.9	6	0.15
<b>Spectral Modes</b>				
S0, No Spectrometer	-	-	-	-
S1, High Spatial/High Spectral	256x336	1.4	1.5	0.93
S2, Medium Spatial/High Spectral	64x336	0.35	1.5	0.23
S3, Low Spatial/High Spectral	16x336	0.09	1.5	0.06

on imager or spectrometer data respectively. The compression is an optional choice and can be commanded accordingly to the observational requirements. Table 6 gives the list of the JIRAM operational sub-modes with uncompressed and compressed data volumes. Two sub-modes, one for the imager and one for the spectrometer will be always combined to create a scientific operation mode. Further considerations about the JIRAM modes are also reported in Table 7. The compression is essentially the reduction of the acquired images to a jpeg format for the imager. The sub-modes denote how the data are pre-elaborated before the transfer from the detectors to the spacecraft, before the downlink. Data from the imager can be simultaneously collected from both the L-band and the M-band sides of the imager (sub-mode I1) or they can be downlinked separately (sub-mode I2 or I3). The compression on the imager data reduces the images of a factor 6. On the other hand, on the spectrometer, an averaging on 4 or 16 contiguous slit pixels can be activated to diminish the data volume of the spectral data. However, this operation leads to a consequent reduction of the spatial resolution and it is applicable when the spatial resolution can be sacrificed for a necessary data volume reduction. Another way to reduce the spectral data volume is through a data compression routine on board the instrument. In this case the compression routine has a limited efficiency due to the fact that, besides compression, the full information contained in the spectral data has to be maintained. The efficacy of the routine depends on the quality of the original data: noisy data lead to the reduction of the compression factor. Furthermore, in presence of a high noise due to thermal reason the routine does not converge to a solution. However, the compression of the data will be applied only in specific cases or possibly never as the allocated data volume budget is now about 2300 *Mbit/orbit*. Then limitations for observation

**Table 7** Characteristics of JIRAM mode and sub-modes under science operations.

MODE	submode hex-code	SUBMODE	# of pixels stored fro IMG	# of pixels stored fro SPE	# of sub-frames
SCI	60 01	I0S1	NO IMG	256 lines 336 samples	IMG=0 SPE = 6
SCI	60 02	I0S2	NO IMG	64 lines 336 samples	IMG = 0 SPE = 3
SCI	60 03	I0S3	NO IMG	16 lines 336 samples	IMG = 0 SPE=3
SCI	60 11	I1S1	256 lines 432 samples	256 lines 336 samples	IMG = 6 SPE = 6
SCI	60 12	I1S2	256 lines 432 samples	64 lines 336 samples	IMG = 6 SPE=3
SCI	60 13	I1S3	256 lines 432 samples	16 lines 336 samples	IMG = 6 SPE = 3
SCI	60 21	I2S1	128 lines 432 samples	256 lines 336 samples	IMG = 3 SPE = 6
SCI	60 22	I2S2	128 lines 432 samples	64 lines 336 samples	IMG = 3 SPE = 3
SCI	60 23	I2S3	128 lines 432 samples	16 lines 336 samples	IMG = 3 SPE = 3
SCI	60 31	I3S1	128 lines 432 samples	256 lines 336 samples	IMG = 3 SPE = 6
SCI	60 32	I3S2	128 lines 432 samples	64 lines 336 samples	IMG = 3 SPE = 3
SCI	60 33	I3S3	128 lines 432 samples	16 lines 336 samples	IMG = 3 SPE = 3
SCI	60 10	I1S0	256 lines 432 samples	NO SPE	IMG = 6 SPE = 0
SCI	60 20	I2S0	128 lines 432 samples	NO SPE	IMG = 3 SPE = 0
SCI	60 30	I3S0	128 lines 432 samples	NO SPE	IMG = 3 SPE = 0
SCI	60 00	I0S0	NO IMG NO IMG	NO SPE NO SPE	IMG = 0 SPE = 0

due both the spinning of the spacecraft and the presence of environmental radiation will oblige JIRAM to be within data volume budget most of the time. JIRAM, depending of the deterioration of its focal plane due to the presence of radiations that will proceed in the course of the mission, could operate as long as all the mission, namely also during the gravity orbits. In those cases because of the constraints imposed by the spacecraft orientation the instru-

ment could only operate in the time period between - 3 hours and + 4 hours from perijove. Figure 47 gives an example of the spectrometer full coverage of

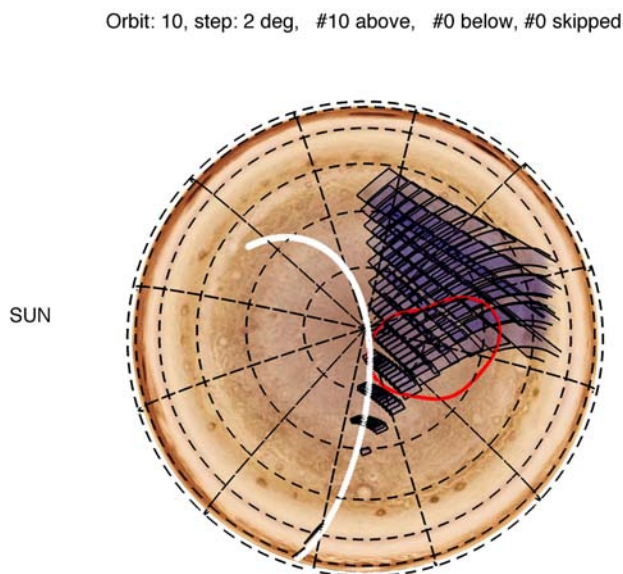


**Fig. 47** Imager coverage on the northern aurora during orbit 10 in the 2 hours before perijove. The blue rectangles are the L-band imager footprints, the white line is the track of the spacecraft on the planet, and the red curve represents the position of the auroral main oval.

the main hot spot latitude bands during orbit 3 and Figure 48 gives the imager coverage on the northern aurora during orbit 10. The period of observation extends from -2 hours from perijove to perijove time.

## 6 JIRAM DATA FORMAT

As already mentioned JIRAM is composed of an imager and a spectrometer. The JIRAM imager data products are images taken on the two different portions of the focal plane of 128 lines by 432 samples size. The JIRAM spectrometer focal plane is composed of 256 spectra (lines) and 336 spectral bands (samples). The spectrometer *FOV* - namely its entrance slit - is partially superimposed (on 256 pixels over 432) to one of the 128 lines of the M-band side of the imager. Figure 49 shows the positioning of the spectrometer slit on the imager. The slit is combined with the line 153 of the imager (as sketched in the figure) and covers the pixels between the 91<sup>st</sup> and the 346<sup>th</sup>.

The instrument is able to operate in two different modes with are respectively the science (SCI) and the calibration (CAL) mode. The CAL mode is orga-

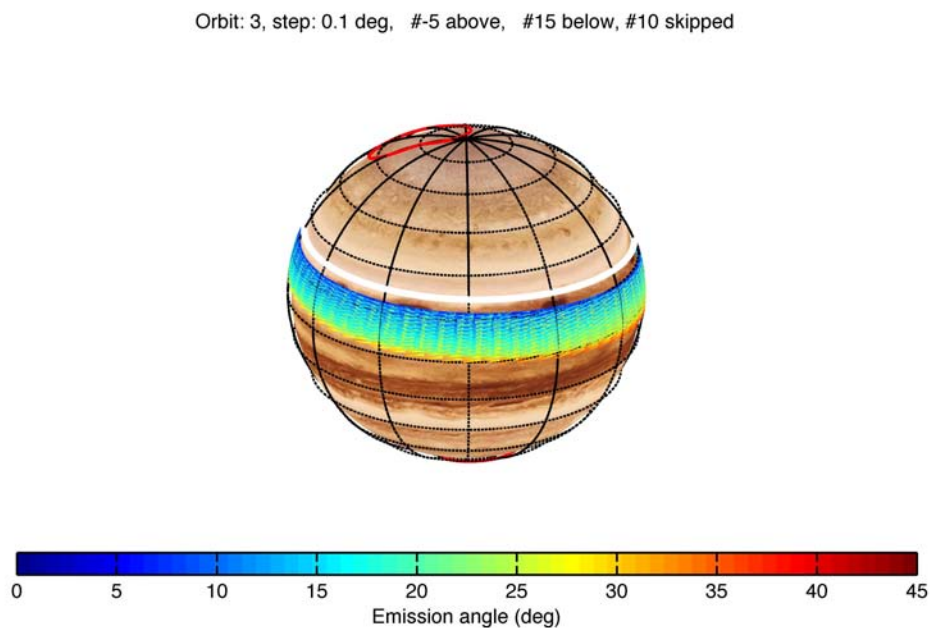


**Fig. 48** Spectrometer coverage of the main hot spot latitude bands during orbit 3. The color area is the spectrometer slit footprint at different emission angles (angles between the normal to the surface and the direction of the spacecraft), the white line is the track of the spacecraft on the planet, and the red curve represents the position of the auroral main oval.

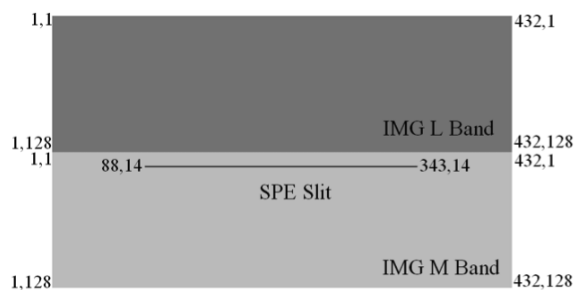


**Fig. 49** Sketch showing the relative correspondences between imager and spectrometer. The numbers represents the coordinates in pixels of the effectively utilized area of the images generated by the JIRAM-IMG. The horizontal line shows the optical position of the spectrometer slit in IMG M Band pixel coordinates.

nized in a sequence of six different measurements, as reported in section 4.10. The SCI mode was developed for scientific observations whose modalities will be set by a number of adjustable parameters. On a regular basis, the acquired data files, related to both focal planes, will be delivered to the spacecraft mass memory once every spin rotation of the spacecraft, during the period

of time in which the instrument is operational. Data will be transmitted to the spacecraft through a fast interface link (HSSL). The HSSL link is doubled for redundancy. Alternatively, in case of failure of both the fast connections, a slow link (LSSL) to the spacecraft can be used with some limitation in the data size.

In the SCI mode the instrument performs a science observation session according to the received parameters. The main tasks are: evaluation of NADIR acquisition time, based on the spacecraft dynamics; instrument commanding; command of the de-spinning mirror motor, to compensate the SC rotation; data pre-processing; data compression; data packing and transmission via HSSL/LSSL to the spacecraft. Several sub-modes are selectable to combine the capabilities of the two IR detectors (the first for images, the second for spectra).

JIRAM data are formatted according to the NASA PDS Data Standards Reference. Currently, two levels of processing are expected for JIRAM data:

- Level 1b, (EDR- Experiment Data Record): telemetry data are cleaned, merged and time ordered according to instrument modes. Data are in scientifically useful form, but still uncalibrated.
- Level 2, (RDR- Reduced Data Records): Level 1b with calibration and corrections applied to yield data in scientific units.

## 6.1 EDR Data Production

The telemetry products, depending on SCI and CAL modes have the characteristics shown in Table 7 and Table 8 respectively. Each Data Product will consist of three files:

1. A binary file containing the scientific telemetry of the instrument, this file is called the Science Telemetry file
2. A binary file containing housekeeping telemetry of the product.
3. A detached ASCII label file describing the content of the data product. Such label is written according to standards defined by the Planetary Data System (PDS), and lists parameters describing both the observation in which data were acquired and the structure of the files in which data are stored and parameters extracted from instrument and spacecraft housekeeping telemetry.

For each data set the JIRAM team will deliver a spreadsheet containing auxiliary information. In each spreadsheet all products are ordered by acquisition time. This file will give an overview on the data set acquisition.

**Table 8** Characteristics of JIRAM mode and sub-modes under calibration operations.

MODE	submode hex-code	SUBMODE	# of pixels stored fro IMG	# of pixels stored fro SPE	# of sub-frames
CAL	50 01	I0S1	NO IMG	256 lines 336 samples	IMG=0 SPE = 6
CAL	50 02	I0S2	NO IMG	64 lines 336 samples	IMG = 0 SPE = 3
CAL	50 03	I0S3	NO IMG	16 lines 336 samples	IMG = 0 SPE=3
CAL	50 11	I1S1	256 lines 432 samples	256 lines 336 samples	IMG = 6 SPE = 6
CAL	50 12	I1S2	256 lines 432 samples	64 lines 336 samples	IMG = 6 SPE=3
CAL	50 13	I1S3	256 lines 432 samples	16 lines 336 samples	IMG = 6 SPE = 3
CAL	50 21	I2S1	128 lines 432 samples	256 lines 336 samples	IMG = 3 SPE = 6
CAL	50 22	I2S2	128 lines 432 samples	64 lines 336 samples	IMG = 3 SPE = 3
CAL	50 23	I2S3	128 lines 432 samples	16 lines 336 samples	IMG = 3 SPE = 3
CAL	50 31	I3S1	128 lines 432 samples	256 lines 336 samples	IMG = 3 SPE = 6
CAL	50 32	I3S2	128 lines 432 samples	64 lines 336 samples	IMG = 3 SPE = 3
CAL	50 33	I3S3	128 lines 432 samples	16 lines 336 samples	IMG = 3 SPE = 3
CAL	50 10	I1S0	256 lines 432 samples	NO SPE	IMG = 6 SPE = 0
CAL	50 20	I2S0	128 lines 432 samples	NO SPE	IMG = 3 SPE = 0
CAL	50 30	I3S0	128 lines 432 samples	NO SPE	IMG = 3 SPE = 0

## 6.2 RDR Data Production

The RDR Data Product consist of a file that contains a PDS binary TABLE-object for spectrometer and a binary IMAGE-object for the imager. Both of them have a detached label describing their structure.



**Table 9** Naming convention for JIRAM products

Product	File Name
Science Data	JIR_SSS_LLL_SCTIME_VVV .EXT JIR_SSS_LLL_SCTIME_VVV .LBL
Housekeeping Data	JIR_LOG_SSS_LLL_SCTIME_VVV .TAB JIR_LOG_SSS_LLL_SCTIME_VVV .LBL
Auxiliary Data	JIR_STATUS_TOT_SCTIME_VVV .CSV JIR_STATUS_TOT_SCTIME_VVV .LBL

**Description:**

SSS indicates the sensor: IMG or SPE  
LLL indicates the processing level, either EDR or RDR.  
SCTIME is yyyydddThmmss  
    yyyy = year  
    ddd = doy  
    hh = hours  
    mm = minutes  
    ss = seconds  
VVV is the version of the data  
EXT is IMG for images and DAT for spectra

### 6.3 File Naming Conventions and Structure

The data are named according to the suffix indicating the channel and the acquisition time. The naming convention for JIRAM products is reported (see also Table 9). All data files in the JIRAM Standard Product Archive Collection have associated detached PDS labels. These label files are named using the same prefix as the data file together with an LBL extension. All spaces and tabulations in the labels are encoded with ASCII character 32 (space). All the labels lines are 80 long, including the EOL marker encoded as ASCII 13-10 (CR-LF). The keywords are grouped in functional sections:

1. Identification Data elements;
2. Mission description parameters;
3. Instrument description parameters;
4. Geometry Information;
  - a. Celestial Geometry,
  - b. Solar Geometry,
  - c. Coordinate System,
  - d. Geometry in 'JUPITER\_FIXED' coordinates from SPICE,
  - e. Channel parameters:
    - Image filter M parameters
    - Image filter L parameters
    - Spectrum parameters,
5. Instrument status;
6. Pointers and Description of the PDS object.

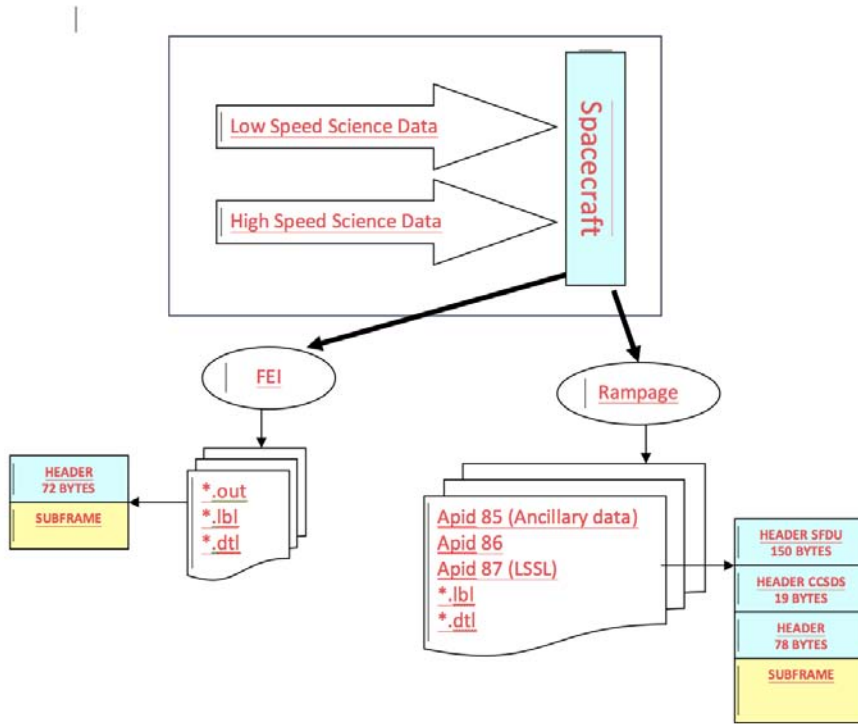


**Fig. 50** JIRAM Raw Science Data Product Pack.

#### 6.4 Downlink Data and Processing Data

The downlink procedures involve JIRAM Science and Engineering Telemetries, as well as JUNO spacecraft housekeeping telemetries and SPICE kernels products. JIRAM is able to transfer the collected data to the spacecraft through two dedicated buses: HSSL and LSSL. Depending on the selected BUS, data products are respectively retrieved by the File Exchange Interface (FEI) for HSSL and RAMPAGE for LSSL (see Figure 50). The data are then fed into the EGSE, located at IAPS-INAF in Rome, and transformed into CODMAC Level 2 data with a detached PDS label (see Figure 51).

#### 6.5 Coordinate Systems

All computations are performed in the planetographic system and using positive westward longitudes in the range 0-360 (longitude increasing with increasing local solar time as the planet rotates). The geographic frame is the one used in the SPICE kernels, and defined in the IAU 2000 system.

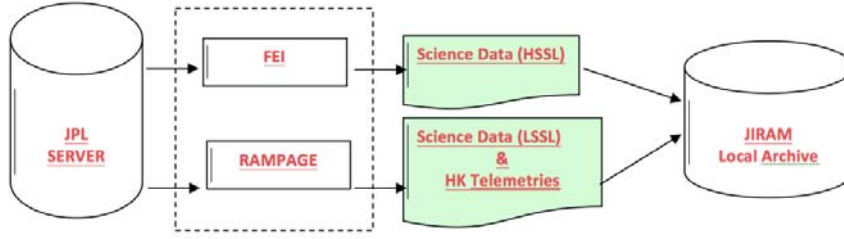


Fig. 51 JIRAM downlink.

## 7 SUMMARY

JIRAM is expected to perform observations for the first part of the mission during orbits identified as MWR, which is the instrument driving the setting of the spacecraft for remote sensing. However, JIRAM will be able to continue to observe the planet during successive scientific orbits driven by a spacecraft orbital setup suitable for gravity measurements, if mission resources are available and until the instrumental degradation due to the harsh radiation environment around Jupiter renders further observations impossible or not useful. Within the temporal and the radiation constraints described in this paper, JIRAM will be able to take measurements on the aurora and the atmosphere, both at nadir, off-nadir and limb viewing geometries.

JIRAM has been built to acquire simultaneously images and spectral information. Among the scientific objectives of the Juno mission, the auroral observations and the deep atmosphere sounding inside hot spots take particular advantage of JIRAM's capabilities. Imaging will permit characterization of the aurora in the infrared range in conjunction with complementary measurements taken by the UltraViolet Spectrometer (UVS) and all the other instruments designed to characterize the Jupiter's magnetosphere and its radiation fields on board Juno. Spectral information will be available to be used for temperature of the thermosphere and column density of the emitting species,  $H_3^+$  and hydrocarbons. The auroral observations are very sensitive to the presence of environmental radiation thanks to the low level of the signal itself. Deeper in the atmosphere and at latitudes different from where the auroral emissions are generated, JIRAM will be able to produce images of the clouds shielding the thermal emission of the planet at different viewing angles by exploiting the band centered around  $5\ \mu m$  wavelength. In particular, in the regions of high thermal emissions, corresponding to the areas defined as hot spots where the atmosphere is relative free of clouds. There, JIRAM spectrometer will be able to sound as deep as 3-5 bars using its spectrometer in the spectral region  $4.6 - 5.0\ \mu m$ . Concentration of some minor gases like water, ammonia and phosphine is expected to be inferred from the measurements in this spectral range.

Through the ground calibrations and tests the optical characterization and the functional verifications of the instrument have been done. The Instrument Transfer Function, *ITF*, has been computed for each pixel of both the spectrometer and the imager. The *ITF* has been implemented in the calibration pipeline to convert the raw data to calibrated data. Both products will be delivered to the NASA PDS for distribution. The knowledge of the *ITF* is also essential information for the forward and inverse retrieval models that will be used in the JIRAM data interpretation. Moreover an accurate measurement of the spectrometer's slit and imager overlaying has been carried out in order to identify with highest precision the imager string of pixel where the spectral and visual information will correspond.

During the cruise to Jupiter a number of tests and internal calibrations are periodically performed to verify the stability of the instrument and its calibration. A milestone during the cruise is represented by the lunar flyby occurring a few hours before the Earth closest approach to happen in October 2013. The lunar fly-by will be used for verification of the radiometric and spectral calibrations. Moreover, that will be the only chance prior the orbit insertion to test the observation sequence that will be used, in a similar manner, at Jupiter. Observations of the Earth will not be possible because of high temperature of the instrument caused by the Earth's albedo.

During each orbit the observation will be complemented by internal calibrations. Background measurements will be frequently taken during each observing sequence in order to quantify the evolution of the background state along the orbit. The background corresponding to each measurement will be removed onboard before the data transmission to the spacecraft for the downlink. Finally, as the JIRAM detectors are sensitive to radiation, periodic background measurements will also be planned use as indirect measurements of the radiation field along the orbit.

## 8 ACKNOWLEDGEMENTS

JIRAM project is funded by the Italian Space Agency presently under contract n. I/010/10/0.

J.I. Lunine's work is supported by a Juno contract from SwRI to Cornell University.

Thanks go to Shawn Kang at JPL for his GEANT4 coding work related to the JIRAM noise predictions.

## References

- Adriani A., A. Coradini, G. Filacchione, J. I. Lunine, A. Bini, C. Pasqui, L. Calamai, F. Colosimo, B. M. Dinelli, D. Grassi, G. Magni, M. L. Moriconi, R. Orosei. *Astrobiology* **8** (3), 613-622 (2008).
- Ammannito E., G. Filacchione, A. Coradini, F. Capaccioni, G. Piccioni, and M. C. De Sanctis, *Rev. Sci. Instrum.* **77**, 093109 (2006).
- Asay-Davis X. S.; P.H. Marcus; M.H. Wong; I. de Pater. *Icarus* **211** (2), 1215-1232 (2011).

- Atreya, S. K. and P.N. Romani in *Recent advances in planetary meteorology*, 17-68, (Cambridge University Press, 1985).
- Atreya, S. K., M. H. Wong, T. C. Owen, P. R. Mahaffy, H. B. Niemann, I. de Pater, P. Drossart, T. Encrenaz. *Planetary and Space Science*. **47**, 1243-1262 (1999).
- Atreya, S.K., Wong, A.S., Baines, K.H., Wong, M.H., and Owen, T.C. *Planetary and Space Science*. **53**, 498-507 (2005).
- Baines K.H., G. Bellucci, J.-P. Bibring, B.J. Buratti, F. Capaccioni, P. Cerroni, R.N. Clark, A. Coradini, D.P. Cruikshank, P. Drossart, V. Formisano, R. Jaumann, Y. Langevin, D.L. Matson, T.B. McCord, V. Mennella, R.M. Nelson, P.D. Nicholson, B. Sicardy, C. Sotin, S. Amici, M. A. Chamberlain, G. Filacchione, G. Hansen, K. Hibbitts, M. Showalter. *Icarus* **164**, 461-470 (2003).
- Baines K.H., Simon-Miller A.A.; Orton G.S., Weaver H.A., Lunsford A., Momary T.W., Spencer J., Cheng A.F., Reuter D. C., Jennings D.E.; Gladstone G. R., Moore J., Stern S.A., Young L.A., Throop H., Yanamandra-Fisher P., Fisher B.M., Hora J., Ressler M.E.. *Science* **318** (5848), 226-229 (2007).
- Banfield D.; Gierasch P. J.; Ingersoll A. P.; Vasavada. A. R.. *Bulletin of the American Astronomical Society* **30**, 1078 (1998).
- Bergin E. A., Y. Aikawa, G. A. Blake, E. F. Van Dishoeck (eds. B. Reipurth, D. Jewitt, K. Keil) in *Protostar and Planets V* (University of Arizona Press, Tucson, USA, 2007).
- Brown R.H., K. H. Baines, G. Bellucci, J.-P. Bibring, B. J. Buratti, F. Capaccioni, P. Cerroni, R. N. Clark, A. Coradini, D. P. Cruikshank, P. Drossart, V. Formisano, R. Jaumann, Y. Langevin, D. L. Matson, T. B. McCord, V. Mennella, E. Miller, R. M. Nelson, P. D. Nicholson, B. Sicardy and C. Sotin. *Space Science Reviews* **115**, 111-168 (2004).
- Carlson R.W., P. R. Weissman, W. D. Smythe, J. C. Mahoney and the NIMS science and engineering teams. *Space Science Reviews* **60**, 457-502 (1992).
- Connerney J. E. P. and T. Satoh. *Phil. Trans. R. Soc. Lond. A*, **358**, 2471-2483 (2000).
- Conrath B. J. and P.J. Gierasch. *Icarus* **67**, 444-455 (1986).
- Coradini A., G. Filacchione, F. Capaccioni, P. Cerroni, A. Adriani, R.H. Brown, Y. Langevin, B. Gondet. *Planetary and Space Science*, **52**, 661-670 (2004).
- Coradini A., F. Capaccioni, P. Drossart, G. Arnold;, Ammannito, E.; Angrilli, F.; Barucci, A.; Bellucci, G.; Benkhoff, J.; Bianchini, G.; Bibring, J. P.; Blecka, M.; Bockelee-Morvan, D.; Capria, M. T.; Carlson, R.; Carsenty, U.; Cerroni, P.; Colangeli, L.; Combes, M.; Combi, M.; Crovisier, J.; De Sanctis, M. C.; Encrenaz, E. T.; Erard, S.; Federico, C.; Filacchione, G.; Fink, U.; Fonti, S.; Formisano, V.; Ip, W. H.; Jaumann, R.; Kuehrt, E.; Langevin, Y.; Magni, G.; McCord, T.; Mennella, V.; Mottola, S.; Neukum, G.; Palumbo, P.; Piccioni, G.; Rauer, H.; B. Saggin, B. Schmitt, D. Tiphene, G. Tozzi. *Space Science Reviews* **128**, 529-559 (2007).
- Coradini A, G. Magni, D. Turrini. *Space Science Reviews* **153**, 411 (2010).
- De Sanctis M.C., A. Coradini, E. Ammannito, G. Filacchione, M. T. Capria ,S. Fonte, G. Magni, A. Barbis, A. Bini, M. Dami, I. Fikai-Veltroni, G. Preti. *Space Science Reviews* **163** (1-4), 329-369 (2011).
- Divine, N. and H.B. Garrett. *J. Geophys. Res.* **88**, 6889-6903 (1983).
- Dullemond C. P., D. Hollenbach, I. Kamp, P. D'Alessio (eds. B. Reipurth, D. Jewitt, K. Keil) in *Protostar and Planets V* (University of Arizona Press, Tucson, USA, 2007).
- Filacchione G., E. Ammannito, A. Coradini, F. Capaccioni, G. Piccioni, and M. C. De Sanctis, *Rev. Sci. Instrum.* **77**, 103106 (2006).
- Filacchione G., PhD Thesis at Università degli Studi di Napoli Federico II. available in Italian at [ftp://ftp.iasf-roma.inaf.it/gianrico/phd/Filacchione\\_PHD\\_2006.pdf](ftp://ftp.iasf-roma.inaf.it/gianrico/phd/Filacchione_PHD_2006.pdf) (2006).
- Friedson A.J. and G.S. Orton, in *DPS Proceedings* (American Astronomical Society, 1999)
- Garrett, H. B., I. Jun, J. M. Ratliff, R. W. Evans, G. A. Clough, and R.W. McEntire *Galileo Interim Radiation Electron Model*. (JPL Publication 03-006, 72 pages, The Jet Propulsion Laboratory, California Inst. of Technology, Pasadena, CA, 2003).
- Garrett, H.B.; S.M. Levin, S.J. Bolton, R.W. Evans, B. Bhattacharya. *Geophys. Res. Lett.* **32** (4), L04104 <http://dx.doi.org/10.1029/2004GL021986> (2005).
- Gierasch P. J., A. P. Ingersoll, D. Banfield, S. P.Ewald, P. Helfenstein, A. Simon-Miller, A. Vasavada, H. H. Breneman, D. A. Senske, and the Galileo Imaging Team. *Nature* **403**, 628630 (2000).
- Gautier D., F. Hersant, O. Mousis, J.I. Lunine. *The Astrophysical Journal* **550**, L227 (2001).

- Guillot, T., B. Gladman, (eds. F. Garzn, C. Eiroa, D. de Winter, and T. J. Mahoney), in *Disks, Planetesimals, and Planets, ASP Conference Proceedings* (Astronomical Society of the Pacific, 2000).
- Guillot T. and R. Hueso. Monthly Notices of the Royal Astronomical Society: Letters **367**, L47-L50 (2006).
- Helled R., P. Bodenheimer P., J.J. Lissauer in *Proceedings IAU Symposium* Eds. Sozzetti A., Lattanzi M. G., Boss A. P. (2011)
- Ingersoll, A. P., Gierasch, P. J., Banfield, D., and Vasavada, A. R. and the Galileo Imaging Team. Nature **403**, 630-632 (2000).
- Ingersoll A. P., T. E. Dowling, P. J. Gierasch, G. S. Orton, P. L. Read, A. Sanchez-Lavega, A. P. Showman, A. A. Simon-Miller, A. R. Vasavada. (Eds. Fran Bagenal, Timothy E. Dowling, William B. McKinnon) *Jupiter. The planet, satellites and magnetosphere*. (Cambridge planetary science, Vol. 1, Cambridge, UK: Cambridge University Press, 2004).
- Irwin, P. G. J.; Weir, A. L.; Taylor, F. W.; Calcutt, S. B.; Carlson, R. W.. Icarus **149**, 397-415 (2001).
- Lindsay, C.M. and B. J. McCall. J. Mol. Spectrosc. **210**, 6083 (2001).
- Limaye, S. S.. Icarus **67**, 342 (1986).
- Lodders, K., Astrophysical Journal **611**, 587 (2004).
- Lunine J. I, A. Coradini, D. Gautier, T.C. Owen, G. Wuchterl, (Eds. Bagenal F., Dowling T., McKinnon W.) *Jupiter - The Planet, Satellites and Magnetosphere*, (Cambridge University Press, UK, 2004).
- Matcheva K.I.; Conrath B.J.; Gierasch P.J.; Flasar F.M.. Icarus **179**, 432-448 (2005).
- Matter, A., Guillot, T., Morbidelli, A., Planetary and Space Science textbf57, 816-821 (2009).
- Mousis O., A. Guilbert-Lepoutre, J. I. Lunine, A. L. Cochran, J. H. Waite, J. M. Petit, P. Rousselot. Astrophysical Journal, **757** (2), (2012).
- Piccioni, G.; Drossart, P.; Suetta, E.; Cosi, M.; Amannito, E.; Barbis, A.; Berlin, R.; Boccacini, A.; Bonello, G.; Bouy, M.; Capaccioni, F.; Cherubini, G.; Dami, M.; Dupuis, O.; Fave, A.; Filacchione, G.; Hello, Y.; Henry, F.; Hofer, S.; Huntzinger, G.; Melchiorri, R.; Parisot, J.; Pasqui, C.; Peter, G.; Pompei, C.; Röss, J. M.; Semery, A.; Soufflot, A.; Adriani, A.; Angrilli, F.; Arnold, G.; Baines, K.; Bellucci, G.; Benkhoff, J.; Bezard, B.; Bibring, J.-P.; Blanco, A.; Blecka, M. I.; Carlson, R.; Coradini, A.; Di Lellis, A.; Encrenaz, T.; Erard, S.; Fonti, S.; Formisano, V.; Fouchet, T.; Garcia, R.; Haus, R.; Helbert, J.; Ignatiev, N. I.; Irwin, P.; Langevin, Y.; Lebonnois, S.; Lopez Valverde, M. A.; Luz, D.; Marinangeli, M.; Orofino, V.; Rodin, A. V.; Roos-Serote, M. C.; Saggin, B.; Sanchez-Lavega, A.; Stam, B. M.; Taylor, F.; Titov, D.; Visconti, G.; Zambelli, M., *ESA Special Publication*, Volume: SP 1295 (ESA, 2007).
- Ortiz J.L., G.S. Orton, A.J. Friedson, S.T. Stewart, and J. Spencer. J. Geophys. Res **103**, 23051-23069 (1998).
- Owen T.C., P. Mahaffy, H.B. Niemann, S. Atreya, T. Donahue, A. Bar-Nun, I. de Pater. Nature **402**, 269-270 (1999).
- Porco C. C.; R.A. West, A. McEwen, A.D. Del Genio, A.P. Ingersoll, P. Thomas, S. Squyres, L. Dones, C.D. Murray, T.V. Johnson, J.A. Burns, A. Brahic, G. Neukum, J. Veverka, J.M. Barbara, T. Denk, M. Evans, J.J. Ferrier, P. Geissler, P. Helfenstein, T. Roatsch, H. Throop, M. Tiscareno, A.R. Vasavada. Science **299** (5612), 1541-1547 (2003).
- Reuter D.C., A. A. Simon-Miller, A. Lunsford, K. H. Baines, A. F. Cheng, D. E. Jennings, C. B. Olkin, J. R. Spencer, S. A. Stern, H. A. Weaver, and L. A. Young. Science **318** (5848), 223-225 (2007).
- Roos-Serote M., S.K. Atreya, M.K. Wong, P. Drossart. Planetary and Space Science **52**, 397-414 (2004).
- Safronov, V. S. *Evolution of the protoplanetary cloud and formation of the earth and planets*. Translated from Russian. Jerusalem (Israel): Israel Program for Scientific Translations, Keter Publishing House, pp. 212 (1972).
- Simon-Miller A.A.; Banfield D.; Gierasch P.J.. Icarus **154**, 459-474 (2001).
- Sromovsky L. A. and P.M. Fry. Icarus **210**, 211-229 (2010a).
- Sromovsky L. A. and P.M. Fry. Icarus **210**, 230-257 (2010b).
- Stoker. C.. Icarus **67**, 106-125 (1986).

- Terrile R. J. and J.A. Westphal. *Icarus* **30**, 274-281 (1977).
- Turrini, D., Magni, G., Coradini, A., Monthly Notices of the Royal Astronomical Society **413**, 2439-2466 (2011)
- Turrini D., Barbieri M., Altieri F., Grassi D., Adriani A., Piccioni G. *EChO Open Science Workshop*, held at ESA-ESTEC (the Netherlands) on July 1-3, 2013.
- Visscher C. and Fegley, B.. *Astrophys. J.* **623**, 1221-1227 (2005).
- Waite Jr. J.H., D. Grodent., B. M. Mauk., T. Majeed., G. R. Gladstone., S. J. Bolton., J. T. Clarke., J. -C. Grard., W. S. Lewis., L. M. Trafton., R. J. Walker., A. P. Ingersoll. and J. E. P. Connerney. *Adv. Space. Res.* **26**, 1453-1475 (2000).
- Walsh K. J., A. Morbidelli, S. N.Raymond, D. P. O'Brien, A. M. Mandell. *Nature* **475**, 206-209 (2011).
- Weidenschilling, S.J. *Icarus* **26**, 361-366 (1975).
- Weidenschilling S. J. and J.S. Lewis. *Icarus* **20**, 465-476 (1973).
- Wong, M. H., P.R. Mahaffy, S.K. Atreya, H.B. Niemann, T.C. Owen. *Icarus* **171**, 153 (2004).